Unique spectral signatures of the nucleic acid dye acridine orange can distinguish cell death by apoptosis and necroptosis

Jason R. Plemel,[1] Andrew V. Caprariello,[1] Michael B. Keough,[1] Tyler J. Henry,[1] Shigeki Tsutsui,[1] Tak H. Chu,[1] Geert J. Schenk,[2] Roel Klaver,[2] V. Wee Yong,[1] and Peter K. Stys[1]

[1]Department of Clinical Neurosciences and the Hotchkiss Brain Institute, University of Calgary, Calgary, AB T2N 4N1, Canada
[2]Department of Anatomy and Neurosciences, VU University Medical Center, 1081 HV Amsterdam, Netherlands

Cellular injury and death are ubiquitous features of disease, yet tools to detect them are limited and insensitive to subtle pathological changes. Acridine orange (AO), a nucleic acid dye with unique spectral properties, enables real-time measurement of RNA and DNA as proxies for cell viability during exposure to various noxious stimuli. This tool illuminates spectral signatures unique to various modes of cell death, such as cells undergoing apoptosis versus necrosis/necroptosis. This new approach also shows that cellular RNA decreases during necrotic, necroptotic, and apoptotic cell death caused by demyelinating, ischemic, and traumatic injuries, implying its involvement in a wide spectrum of tissue pathologies. Furthermore, cells with pathologically low levels of cytoplasmic RNA are detected earlier and in higher numbers than with standard markers including TdT-mediated dUTP biotin nick-end labeling and cleaved caspase 3 immunofluorescence. Our technique highlights AO-labeled cytoplasmic RNA as an important early marker of cellular injury and a sensitive indicator of various modes of cell death in a range of experimental models.

Introduction

Cell injury and death are a fundamental aspect of disease, yet techniques to visualize these processes in fixed tissue are limited; techniques are available to visualize apoptotic cells, but few techniques permit the visualization of cellular injury and nonapoptotic forms of death. Because of the diverse modes of cell death, and because sublethal injury may not irreversibly lead to death, examining apoptosis alone provides an incomplete picture of pathology (Abend, 2003). Furthermore, although there are more options to detect viability in vitro, measuring cell death in fixed tissue must rely on stable ultrastructure or chemical changes that are unaffected by fixation (Taatjes et al., 2008; Vanden Berghe et al., 2013). DNA fragmentation is a feature of apoptosis and can be measured by antibodies directed against single-stranded DNA (Frankfurt and Krishan, 2001) or TUN EL (Gavrieli et al., 1992). Another means to determine apoptosis is by the presence of caspase cleavage products (Gown and Willingham, 2002); however, caspase-independent forms of cell death exist and can be an important feature of disease, such as with oligodendrocyte injury in early multiple sclerosis lesions (Barnett and Prineas, 2004; Henderson et al., 2009). Perhaps the most instructive means to detect cell death is with electron microscopy, as it allows direct visualization of the ultrastructure of apoptotic and necrotic cells (Wyllie et al., 1980). However, electron microscopy is time-consuming and challenging for quantitative assessments. The requirement for new tools will only increase with the discovery of a programmed necrosis dependent on receptor-interacting protein kinase 3 (RIPK3), referred to as necroptosis (Degterev et al., 2005; Linkermann and Green, 2014). Already, necroptosis is involved in a wide range of conditions ranging from ischemic brain injury (Degterev et al., 2005) to multiple sclerosis (Ofengeim et al., 2015).

New strategies to better visualize cell death in fixed tissue would be very valuable and would ideally provide new chemical information reflecting the injury process. Although it is well described that DNA is degraded during cell death, it is less recognized that there is also attendant RNA loss (Cidlowski, 1982; King et al., 2000; Del Prete et al., 2002). With this in mind, we used spectral microscopy to measure fluorescence patterns of the nucleic acid–sensitive dye acridine orange (AO), in vitro and in vivo. By analyzing the fluorescence emission spectra of AO, we provide a ratiometric measure of nuclear and cytoplasmic RNA, yielding a continuous metric that is very sensitive to pathology. We also find that distinct AO fluorescence can distinguish between apoptotic insults and necrotic/necroptotic mechanisms of

Correspondence to Peter K. Stys: pstys@ucalgary.ca

Abbreviations used: ANOVA, analysis of variance; AO, acridine orange; CC3, cleaved caspase 3; CPZ, cuprizone; LPC, lysophosphatidylcholine; MAG, myelin-associated glycoprotein; PI, propidium iodide; PLL, poly-L-lysine; RIPK, receptor-interacting protein kinase; SCI, spinal cord injury.

The Rockefeller University Press $30.00
J. Cell Biol. Vol. 216 No. 4 1163–1181
https://doi.org/10.1083/jcb.201602028

cell death. We show that RNA loss in fact precedes commonly used markers of death, making RNA measurement using spectral confocal microscopy of AO a new and highly informative characteristic to monitor various forms of cellular injury.

Results

RNA is an essential molecule of all living organisms that could theoretically provide reliable information on cellular injury. To determine how RNA changes during cellular injury, we used the fluorescent nucleic acid dye AO (Tomita, 1967; Traganos et al., 1977; Löber, 1981; Kapuscinski et al., 1982). To define the unique spectral properties of AO, we first measured its spectral characteristics in aqueous solution (Fig. 1, a and b). At a relatively low concentration and without exogenous nucleotides, AO had a single green emission peak (∼530 nm) that was unaltered by the addition of proteins (0.1% albumin). In contrast, DNA induced an ∼10-nm blue shift of the longer-wavelength components. In the presence of AO, RNA is known to form insoluble complexes above a certain dye:RNA ratio (Kapuscinski et al., 1982). Similarly, we found that when RNA was present in the 50-µM AO solution it formed precipitates that exhibited a second, unique, red-shifted spectral peak centered at ∼635 nm (Fig. 1, a and b). AO alone at higher concentrations (200 and 500 µM) displayed spontaneous red emission at ∼650 nm (Fig. 1, c and d). At these higher AO concentrations, both nucleic acids stimulated an increase in red emissions (Fig. 1, c and d). Therefore, RNA can best be distinguished from DNA at lower dye concentrations (50 µM) by a red peak at ∼635 nm.

To ensure that the red emission reflected RNA in intact cells, a human oligodendrocyte cell line (MO3.13 cells) was fixed and stained with AO. Consistent with RNA-rich cytoplasm and nuclear bodies, when stained with AO, these cells exhibited diffuse red staining throughout the cytoplasm and a distinctly green nucleus containing red punctate structures (Fig. 1 e). Although both cytoplasm and nuclei contained red AO signal, the cytoplasmic red signal was much more prevalent relative to the nucleus (Fig. 1 f). To confirm that the red spectral peak in AO-stained MO3.13 cells was RNA-related, cells were treated briefly with a detergent to permeabilize membranes and then exposed to RNase or PBS. Consistent with sensitivity for RNA, RNase largely eliminated the red AO emission in the nucleus and cytoplasm alike, although the effect was more prominent in the cytoplasm. We measured red emissions in the nucleus because the boundaries of nuclei were easy to identify. Nuclear red AO signal significantly decreased over time compared with PBS controls (Fig. 1, g–i). Collectively, our results show that the spectral properties of AO reliably identify cellular and nuclear RNA in vitro.

There are other benefits of AO that make it useful experimentally. Because AO has a long Stokes shift, distinct red and green emission patterns can be captured using excitation filters, making the imaging of red and green AO emission possible using traditional fluorescent microscopy (Fig. 1 j). Given the strong DNA-dependent green component of AO fluorescence, an added benefit is the ability of this probe to clearly label nuclei, allowing easy cell identification; Fig. 1 (k and l) shows the identical staining pattern of green AO emission and the traditional nuclear dye DAPI.

To characterize RNA changes according to established methods during various modes of cell death, we used a live/dead assay in primary cultures of oligodendrocytes. These cells are damaged in many neurological disorders, and oligodendrocyte death is an early feature of a subset of multiple sclerosis lesions (Barnett and Prineas, 2004; Henderson et al., 2009). We developed murine oligodendrocyte cultures with ∼80% purity that had >75% survival after 5 d in vitro, demonstrating their long-term stability in culture (Fig. S1). We next exposed oligodendrocytes to four toxins that promote cell death by different mechanisms: H_2O_2 induces caspase-3–independent cell death, producing a mixture of apoptosis and necrosis (Richter-Landsberg and Vollgraf, 1998; Fragoso et al., 2004); lysolecithin (lysophosphatidylcholine [LPC]) is a detergent that permeabilizes cell membranes, thus mimicking necrosis; staurosporine is a broad-spectrum protein kinase inhibitor that robustly induces oligodendrocyte apoptosis (Richter-Landsberg and Vollgraf, 1998; Scurlock and Dawson, 1999); and rotenone blocks the electron transport chain and hence oxidative phosphorylation by the mitochondria, resulting in enhanced reactive oxygen species–induced cell death (Barrientos and Moraes, 1999; Li et al., 2003).

To define baseline cell viability in vitro after treatment with toxins, we exposed cells to the cell-permeant live-cell indicator calcein AM. Upon entering a living cell, cellular esterases cleave the AM group, trapping the fluorescent calcein within the cell, thus giving a measurement of cellular metabolic activity and integrity of the cell membrane. We also used a second viability indicator, propidium iodide (PI), which is a nuclear dye that can enter cells only upon membrane disruption present during primary or secondary necrosis. Using PI and calcein AM to assess dead cells in oligodendrocyte cultures, we found substantial cell death after 3-h exposure to 200 µM LPC and 6-h exposure to 1 mM H_2O_2 or 50 nM staurosporine (Fig. 2, a–f). Rotenone induced cell injury at a slower rate (Fig. 2, g and h). Importantly, with all toxins, the vast majority of cells were dead after 24 h.

To ascertain how diverse cell death mechanisms differentially induce changes in AO—and hence RNA— fluorescence, we next correlated AO emission spectra with the established time course of death with these four toxins. Recognizing that the red, RNA-dependent peak might be a more sensitive readout of cellular injury, we used the ratio of the red to the green peak intensity from the nucleus as a ratiometric measure that is largely independent of absolute signal intensity, which is notoriously difficult to control in fluorescence microscopy. Similar to MO3.13 cells, healthy oligodendrocytes fixed and stained with AO had red cytoplasmic and mixed red/green nuclear staining patterns (Fig. 2 i). After exposure to toxins for 24 h, red cytoplasmic staining was greatly diminished, and nuclei had less red signal within them as well (Fig. 2, j–m). After 6 h of exposure to H_2O_2, staurosporine, and rotenone and 3 h of exposure to LPC, we found a significantly reduced nuclear red peak (Fig. 2, n–q). For each of these toxins, the reduced nuclear red peak occurred at the same time as the increase in cell death as measured by conventional markers (Fig. 2, a–h). Similarly, cells that displayed morphological characteristics of cell death under control conditions also had a reduced AO nuclear red signal (Fig. S2). These findings were also generalizable to MO3.13 cells, in which decreased red staining from cytoplasm and nucleus coincided with enhanced cell death as reported by established markers (Fig. S3); AO changes preceded PI entry, suggesting that AO may be a more sensitive marker of cellular injury (Fig. S3). Thus, in cultured oligodendrocytes and MO3.13 cells, the change in AO staining was a reliable indicator of cell death/injury.

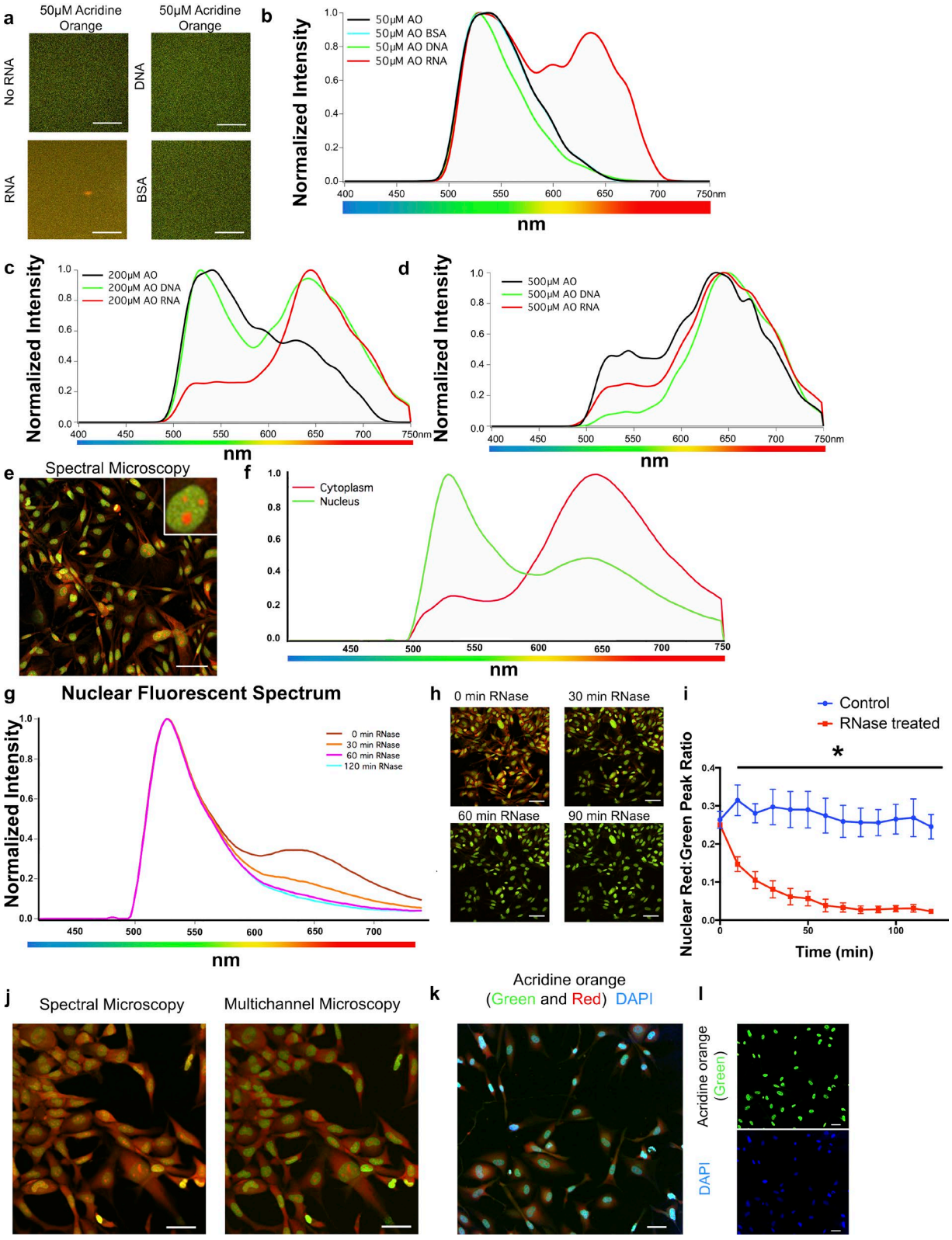

Figure 1. **At low concentrations, the red emission of AO is specific to RNA.** (a and b) 50-μM AO solutions with isolated DNA, RNA, or BSA indicate distinct AO spectral peaks for the nucleic acids but not protein; the red peak at ~650 nm was specific for RNA. (c and d) Higher concentrations reduced the specificity of the red peak and even induced a red peak in the absence of added nucleic acids. (e and f) Fixed MO3 cells stained with AO have distinct spectral characteristics in the nucleus and cytoplasm. (g–i) Cytoplasmic and nuclear red AO emission is RNase sensitive. Fixed MO3.3 cells stained with AO were Triton permeabilized and treated with RNase, which significantly decreased the red emission over time. (j) Example image was taken using both spectral and multichannel settings. (k and l) Multichannel image capturing green and red emission from AO-labeled cells demonstrates green AO emission colabeling with DAPI. Bars, 50 μm. Data are shown as mean ± SEM. Each data point represents six wells. Data were analyzed with two-way ANOVA using Sidak's multiple comparison to compare control with RNase-treated groups at each time point.

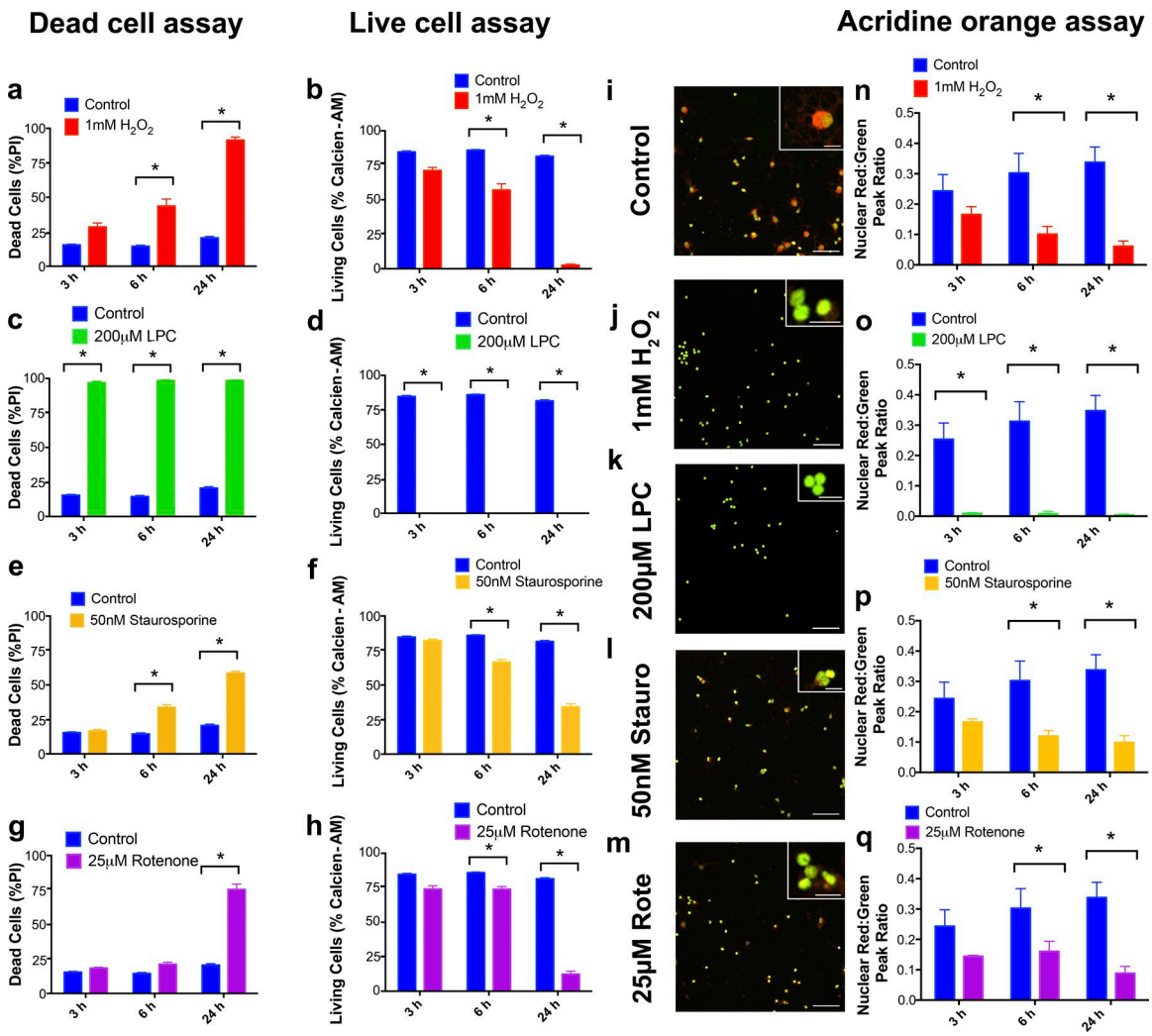

Figure 2. **Oligodendrocyte death induced by four different insults resulted in decreased RNA content as reported by reduced red AO emission.** (a–h) Live/dead results from oligodendrocytes pulsed with H_2O_2 (a and b), LPC (c and d), staurosporine (Stauro; e and f), or rotenone (Rote; g and h). (i–m) Representative spectral confocal images from all four injury conditions. 24 h after toxin exposure, AO-stained oligodendrocytes lost red signal from nucleus and cytoplasm. (n–q) Bar graphs summarizing nuclear AO emission (as ratios of red vs. green peak intensities) after 3-, 6-, and 24-h toxin exposure. In all cases, the decreased red emission paralleled diminished viability measured by standard techniques. Bars: 50 µm; (inset) 10 µm. Data are shown as mean ± SEM. Each data point represents a minimum of two biological replicates, each with a minimum of three wells. Data were analyzed with two-way ANOVA using Sidak's multiple comparison test against control values (*, significant difference compared with control at given time point).

During injury, reduction of red AO signal was also closely matched by cellular membrane retraction (Fig. S4). Red AO emission in healthy cells is found throughout the cytoplasm compared with a cellular membrane stain; during injury, cell membranes retracted, as did cytoplasmic red AO labeling. Only in severely compromised cells injured by H_2O_2 did cell membranes occupy a larger area than red AO signal. Reduced red AO emission therefore also reflects a retracted cellular membrane.

Nuclear RNA is not homogeneously distributed within the nucleus but instead is differentially organized into nuclear bodies (Mao et al., 2011; Dundr, 2012). Given our findings that nuclear RNA reduction reflects oligodendrocyte cell injury/death, we developed a novel analytical tool to reliably quantify spectral changes in an unbiased manner. Fluorescence images acquired with spectral detectors are divided into 3 × 3–pixel "kernels" to provide averaging of the inherently noisy single-pixel spectra. To numerically quantify AO spectral shifts, two reference spectra were generated from low- and high-RNA regions of a control sample stained with AO (Fig. 3 a). A continuous index ranging from 0 to 1 was calculated for each kernel, reflecting how closely its spectral shape approximated either of the two limiting bracketing spectra: an index of 0 represents a healthy AO spectrum that was RNA enriched (i.e., contains substantial red emission), whereas an index of 1 reflects a pathological AO spectrum that was low in RNA, as in injured cells. A cumulative histogram of kernel indexes readily identified whether a sample was enriched in lower-index (healthy) versus higher-index (sick) kernels. To determine how oligodendrocyte toxicity impacted its nuclear AO spectral properties, we measured AO index changes 3, 6, and 24 h after toxic exposure to H_2O_2, staurosporine, rotenone, and LPC. In all conditions, there was a consistent shift toward high, pathological indexes, indicative of lower RNA levels and a greater degree of injury (Fig. 3, b–j). Calculating index changes provides a sensitive and quantitative tool to measure the continuum of AO spectral changes; we found that in cultured oligodendrocytes, a shift toward higher indexes coincided with cell injury/death.

In addition to capturing the heterogeneity of changes within nuclei, the sensitivity of the index-based analysis can

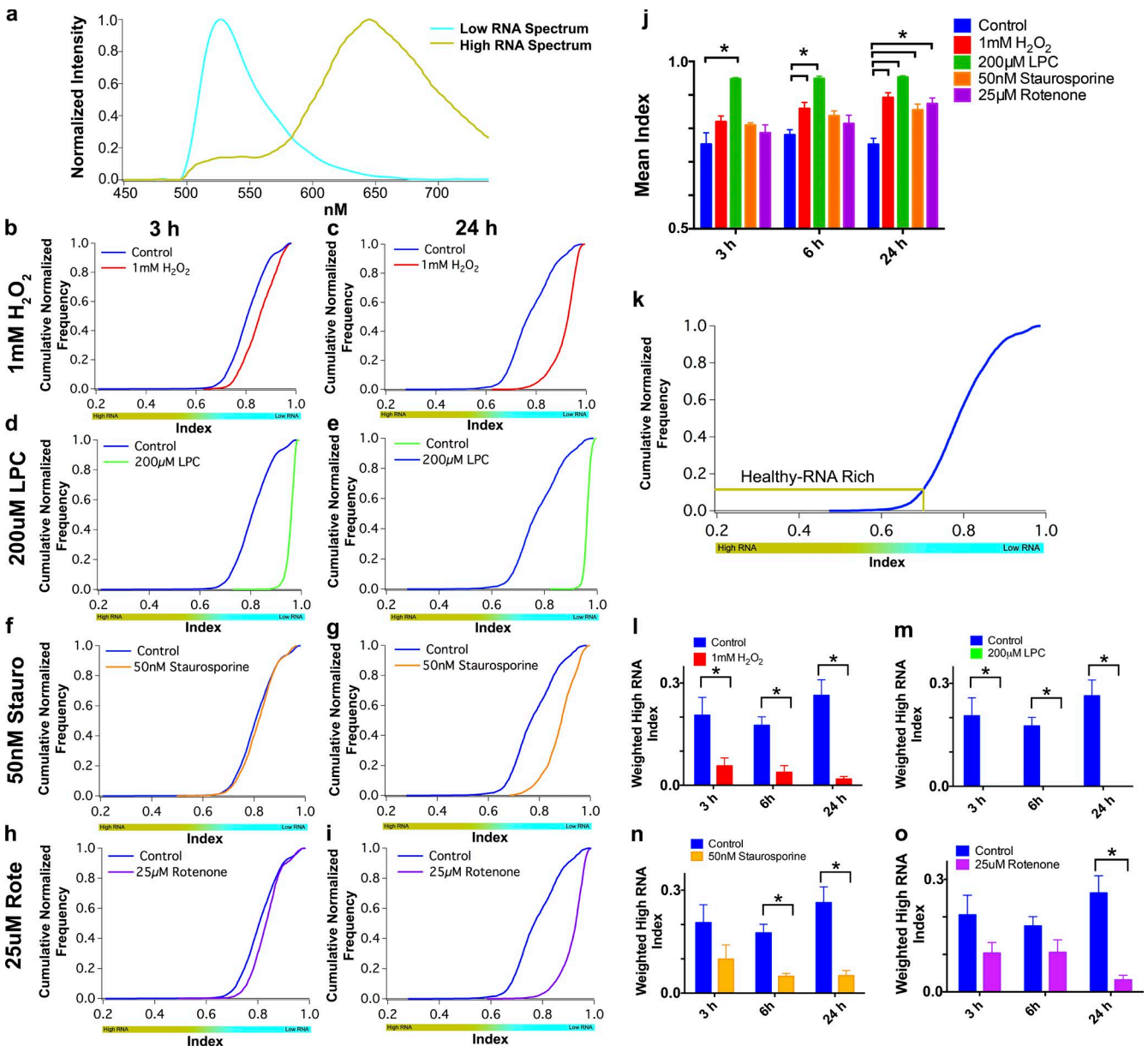

Figure 3. **Quantitation of spectral micrographs based on spectral shifts of AO fluorescence.** (a) An index was calculated at each location of an image reflecting its spectral shape; low- versus high-RNA signatures were assigned a continuous value between 0 and 1 (see Materials and methods). (b–j) As oligodendrocytes died, there was a shift in AO spectra within nuclei toward lower RNA values/higher indexes, presented as cumulative normalized frequency histograms (b–i); more right-shifted distributions indicate more cellular injury. Toxic exposure to H_2O_2 (b and c), LPC (d and e), staurosporine (Stauro; f and g), or rotenone (Rote; h and i) induced a consistent shift to higher indexes, indicating injury measured in a quantitative manner (j). (k) To increase sensitivity, analyses were then repeated using a subrange of indexes favoring less-injured kernels, because these disappeared most quickly with applied insult (gold box). (l–o) The index of these kernels as a proportion of the total number of nuclear kernels was calculated; lower values indicate more injury. These parameters were used as a sensitive surrogate marker for cell injury and death. Each data point represents a minimum of two independent experiments, each with a minimum of three wells each. Data are shown as mean ± SEM. Data were analyzed with two-way ANOVA using Sidak's multiple comparison test against control values (*, significant difference compared with control at given time point).

be further enhanced by considering subsets of kernel distributions (Fig. 3 k). Rather than calculating aggregate means from all kernels as in Fig. 3 j, statistics were instead calculated on kernels within an index range that pertained to less damaged cellular nuclei (lower index values); index values were calculated as the proportion of kernels within a given range compared with the total number of nuclear kernels. Toxin exposure decreased the proportional index of kernels within the selected RNA-rich index range, indicating that there were fewer kernels with a healthy RNA-rich status (Fig. 3, l–o). For example, oligodendrocytes treated with H_2O_2 had a reduced proportional index at 3 h, indicating a significant cellular injury that was not evident by conventional methods in which the percentage of living or dead cells was measured (Fig. 2, a and b, vs. Fig. 3 l). Thus, subtle changes within a given index range detected early alterations that were not detected by calcein AM or PI staining, emphasizing the usefulness of the graded changes reported by our method.

Given the RNase sensitivity of AO's red signal as well as previous data supporting its ability to identify cell viability, we

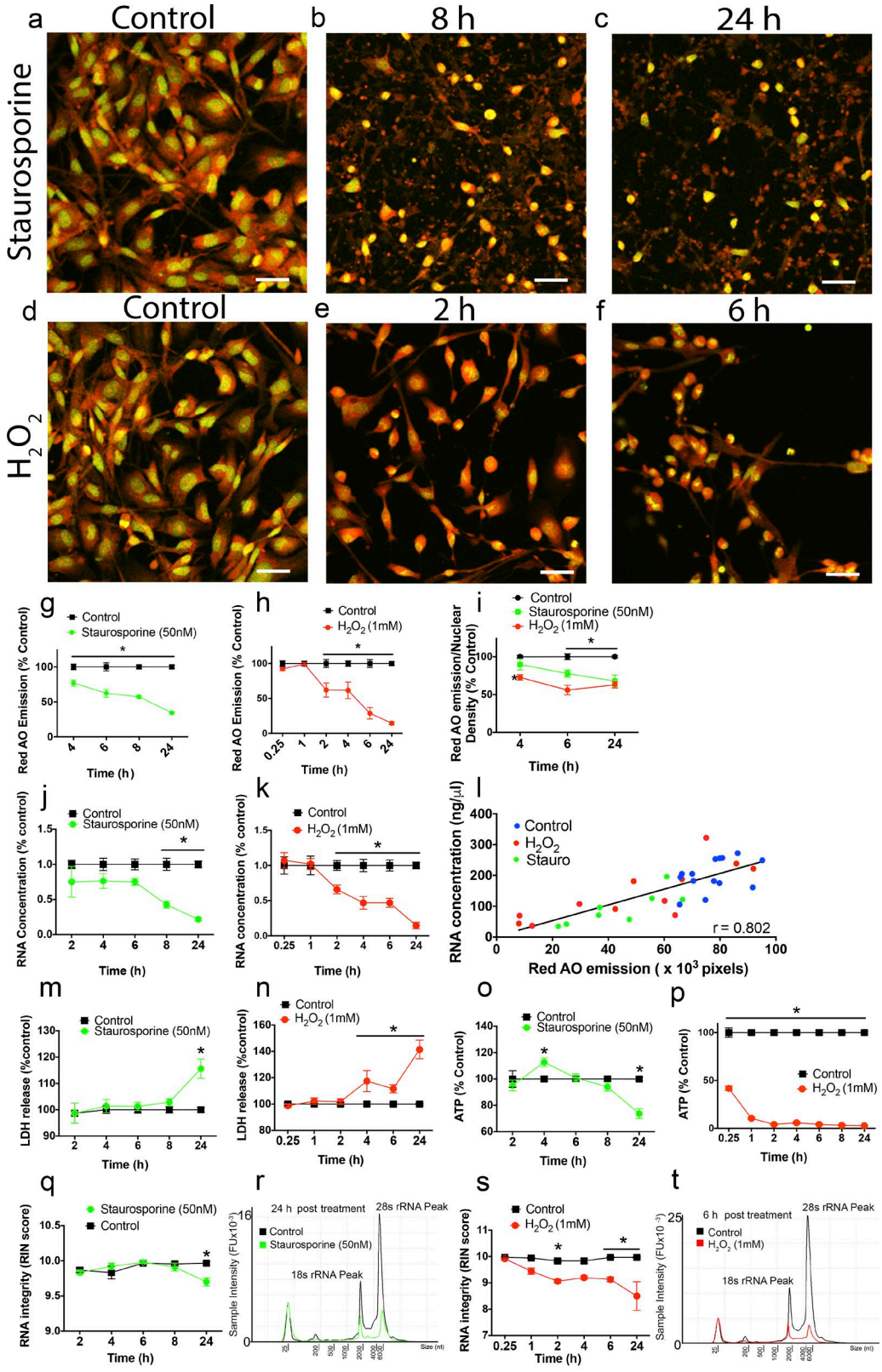

Figure 4. **Red AO emission mirrors RNA levels, both of which decline during cell death.** (a–f) Representative spectral confocal images taken from cells under control conditions (a and d) compared with cells treated for 8 (b) and 24 (c) h with staurosporine and for 2 (e) and 6 (f) h with H_2O_2. (g–i) In MO3 cells, red AO emission and red AO emission per nuclear region both decreased after staurosporine (g and i) and H_2O_2 (h and i) treatments. (j and k) RNA collected from parallel cultures under identical conditions mirror the drop in red AO signal after staurosporine (j) and H_2O_2 (k) treatment. (l) The concentration of RNA is strongly correlated with red AO emission. (m–p) After staurosporine (m and o) and H_2O_2 (n and p) treatment, there was an increase in cell membrane permeability (m and n) measured by extracellular release of LDH and a decrease in cellular energy measured with intracellular ATP levels (o and p). (q–t) Cell death ultimately lowers RNA integrity (RIN score) after staurosporine (q and r) and H_2O_2 (s and t) exposure, outlined with representative

wished to confirm that changes in AO reflected genuine RNA differences. MO3.13 cells were pulsed with either 1 mM H_2O_2 or 50 nM staurosporine under otherwise identical conditions; these toxins were chosen to reflect different modalities of cell death (Fig. 4). At several time points after toxin exposure, cells were fixed and stained with AO and compared with parallel cultures in which RNA was extracted. Importantly, RNA concentration was strongly correlated with red AO emission (r^2 = 0.64). Irrespective of the mode of cell death (Fig. 4, g and h), the toxin-induced decrease in red AO signal was mirrored strongly by reductions in RNA concentration, consistent with the RNA sensitivity of AO (Fig. 4 l). Moreover, decreases in both AO and RNA preceded cell membrane permeability (Fig. 4, m and n). These data indicate that AO's spectral properties are a reliable proxy for RNA changes and provide a more sensitive assessment of cellular injury/death than traditional methods.

We hypothesized that the loss of RNA reflected metabolic decline; however, this proved not necessarily true: cellular ATP was not significantly reduced until 24 h after staurosporine treatment, whereas RNA differences were reduced by approximately half by 8 h (Fig. 4 o). With staurosporine treatment, RNA integrity—indicated by its RNA integrity number (RIN) score (Imbeaud et al., 2005)—remained high during periods of RNA loss (Fig. 4, q and r). In contrast, H_2O_2 treatment reduced cellular ATP levels 15 min after treatment; thus under these conditions, it could be in part responsible for the drop in RNA observed 2 h later (Fig. 4 p). Consistent with metabolic dysfunction driving RNA loss with H_2O_2 treatment, there was a drop in RNA integrity at 2 h that mirrored the overall loss of RNA (Fig. 4, s and t). Collectively, the apoptotic cell death initiated by staurosporine resulted in RNA loss without any measured drop in RNA quality or cellular energy levels, consistent with data suggesting active RNA degradation during apoptosis (Mondino and Jenkins, 1995; Del Prete et al., 2002; Bushell et al., 2004; Padmanabhan et al., 2012). The increase in necrotic cell death caused by H_2O_2 treatment resulted in an early metabolic decline, followed 2 h later by a drop in RNA integrity and RNA concentration, suggesting that metabolic decline might drive RNA loss during necrosis.

We next wanted to determine whether AO spectral patterns might be useful in distinguishing different cell death mechanisms, namely apoptosis, necrosis, and necroptosis. Because MO3.13 cells do not undergo necroptosis (unpublished data), we used two different fibroblast lines (mouse embryonic fibroblasts [MEF] and NIH 3T3 cells) that are known to undergo such injury (Moujalled et al., 2013; Sosna et al., 2013; Seo et al., 2016). To induce apoptosis, MEF and NIH 3T3 cells were treated with staurosporine (Fig. 5, e and m). Staurosporine-induced cell death was present 24 h after treatment and was mitigated by the pan-caspase inhibitor zVAD-FMK, but not by necrostatin, an inhibitor of RIPK1 that targets necroptotic cell death. Thus, staurosporine induced fibroblast cells to undergo apoptosis and not necroptosis. Moreover, staurosporine increased caspase activity in these cells (Fig. 5, f and n). To induce necrosis, MEF and NIH 3T3 cells were treated with high concentrations of H_2O_2 (1 mM); this treatment was attenuated by neither caspase inhibition nor necrostatin exposure, suggesting that at these levels H_2O_2 induced a RIPK1-independent necrosis (Fig. 5, g and o).

Necroptosis is a RIPK3-dependent programmed necrosis that is classically induced with TNF and a pan-caspase inhibitor (Vercammen et al., 1998; Linkermann and Green, 2014). Here, fibroblast cells were treated with TNF along with a pan-caspase inhibitor (Fig. 5, h and p), which induced cell death in both fibroblast cell lines, but 3T3 cells were much more responsive (~91% mortality at 24 h) compared with MEFs (~38% mortality). In both fibroblast cell lines, cell death was prevented by necrostatin for 6 h, indicating that TNF and caspase inhibition induced necroptosis in these fibroblast lines.

To determine whether fibroblast cells undergoing different cell death mechanisms exhibit unique AO spectral patterns, cells were pulsed with staurosporine to induce apoptosis, H_2O_2 to induce necrosis, and TNF with caspase inhibition to induce necroptosis (Fig. 6). After 6 and 24 h, cells were fixed and stained with AO. Healthy cells in control conditions had a flattened morphology observable by cytoplasmic red AO emission; these cells had a clearly demarcated nucleus with enriched red signal lining the entirety of the nucleus (Fig. 6, i–k). After 6 h of staurosporine exposure, fibroblasts no longer possessed a flattened morphology but instead had thin processes with cellular fragmentation. As red AO signal diminished, cells lost remaining processes, no longer contained a clear nuclear demarcation, and had a shrunken nucleus. Late stages of apoptosis could be distinguished by the nearly complete absence of red AO signal and the fragmentation and condensation of nuclei that were easily distinguished by their irregular outline.

In contrast to apoptosis, necrosis and necroptosis had several unique morphological attributes that were very similar to one another (Fig. 6, l–p). During early stages of necroptosis and necrosis, there was an overall loss of red AO structure caused by cellular shrinkage, but there were no signs of cellular fragmentation. These early signs of necrosis/necroptosis included nuclear shrinkage and a loss of nuclear demarcation. At the final stages of necrosis/necroptosis, the nuclei were small and spherical and often had an increase in intensity or a smooth ungranulated appearance. Such nuclei had little cytoplasmic red AO signal. Thus the lack of cytoplasmic and nuclear fragmentation—both observed with apoptosis—along with the persisting smooth round nucleus lacking cytoplasmic red AO emission was sufficient to distinguish necrosis/necroptosis from apoptosis. Because green AO emission reflects DNA changes and red AO emission is sensitive to RNA, we found that different mechanisms of cell death can be distinguished based on changes in the morphological distribution of these two different classifications of nucleotides.

AO thus provides a spectral signature that represents changes to RNA and illuminates very early cell injury and cell death in vitro with great sensitivity. However, cells in culture lack the 3D organization found in tissue. To determine the utility of this probe with fixed tissue, spinal cord sections were

electropherograms demonstrating RNA quality at 24 h after treatment (r and t). Data points represent two to three independent experiments, each with a minimum of three wells. Bars, 50 µm. Data are shown as mean ± SEM. Data were analyzed with two-way ANOVA using Sidak's multiple comparison test (g, h, j–q, and s) or Dunnett's multiple comparison test against control values (i) (*, significant difference compared with control at given time point). Each data point in the correlation analysis represents a mean value from an experimental time point. Correlations were significant ($P < 0.0001$), and r^2 was determined using Pearson's correlation (l).

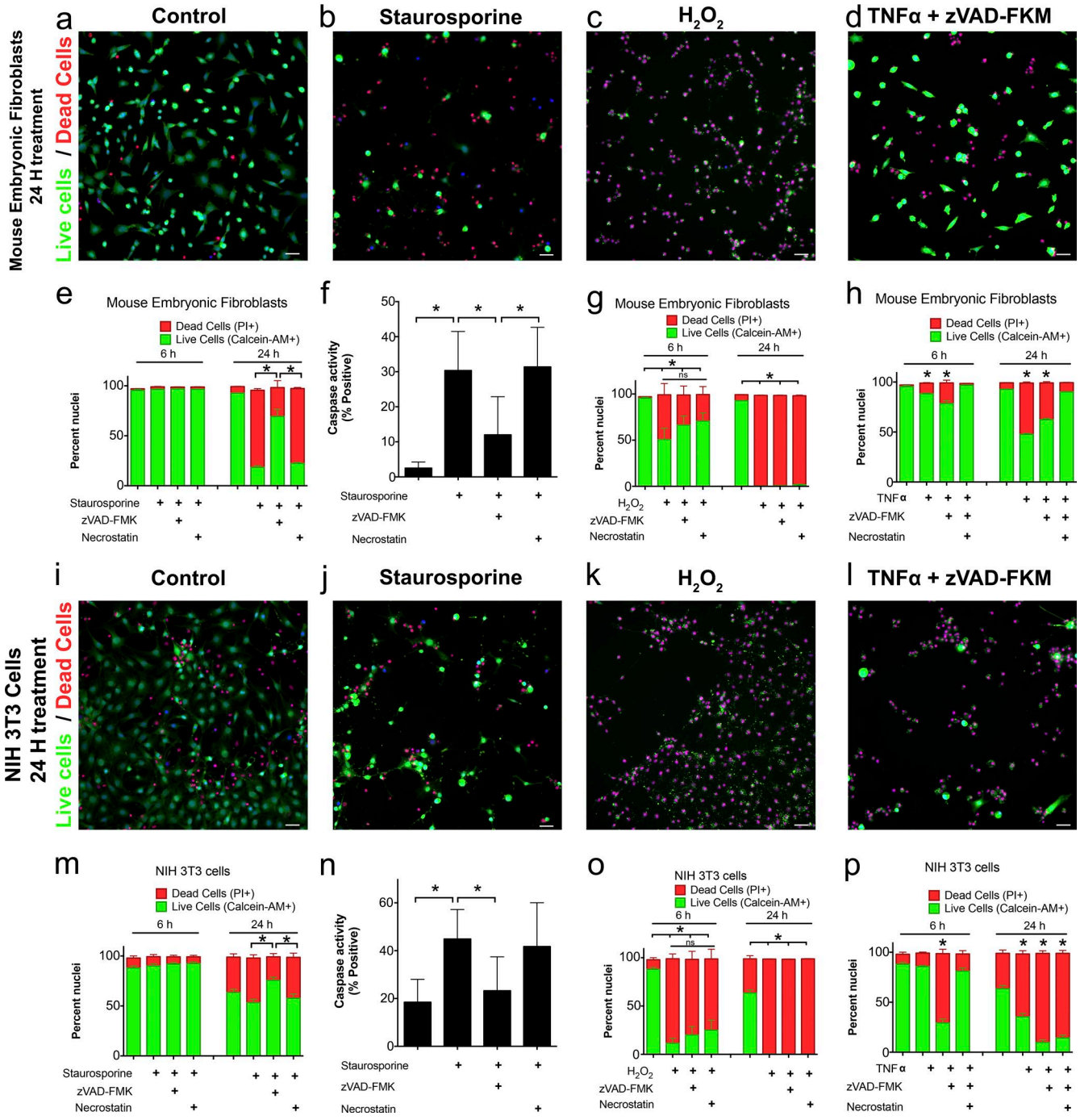

Figure 5. **Apoptotic, necrotic, and necroptotic cell death can be induced in MEF and 3T3 NIH cells using staurosporine, H_2O_2, and TNF/zVAD-FMK, respectively.** (a–d and i–l) Representative images of MEF cells (a–d) or 3T3 cells (i–l) stained with calcein AM (green), PI (red), and NucBlue (blue) that were either untreated (a and i) or treated with staurosporine (b and j), H_2O_2 (c and k), or TNF/zVAD-FMK (d and l). (e–h and m–p) Bar graphs represent treatment of MEF cells (e–h) or 3T3 NIH cells (m–p) with staurosporine (e and m), H_2O_2 (g and o), or TNF/zVAD-FMK (h and p) to induce cell death. Apoptosis, defined as caspase-responsive cell death inhibited with a pan-caspase inhibitor zVAD-FMK, occurred only with staurosporine. Consistent with apoptosis induction, caspase 3/7 activities were increased after staurosporine treatment in MEF cells (f) and 3T3 NIH cells (n) as detected using a fluorescent probe. Necroptosis, defined by sensitivity to the RIPK1 inhibitor necrostatin, occurred only with TNF/zVAD-FMK-induced cell death. H_2O_2-induced necrosis was defined by its insensitivity to caspase inhibition and necrostatin. Bars, 50 µm. Data are shown as mean ± SEM. Data were analyzed with two-way ANOVA using Tukey's multiple comparison test (e–h and m–p). *, Difference from control value unless designated otherwise.

stained with 50 µM AO and spectral images were acquired. Healthy cells contained predominantly green nuclei and a red cytoplasmic ring; this high red emission was localized within the cytoplasm, consistent with RNA localization (Fig. 7, a and b). As with cultured cells, tissue treated with RNase exhibited a decrease in the nuclear red spectrum compared with PBS-treated sections (Fig. 7, c–e). Further confirmation that DNA can be measured with green AO signal and RNA with red AO signal comes from the specific colabeling of green AO emission with the specific DNA dye DAPI and colabeling of red AO

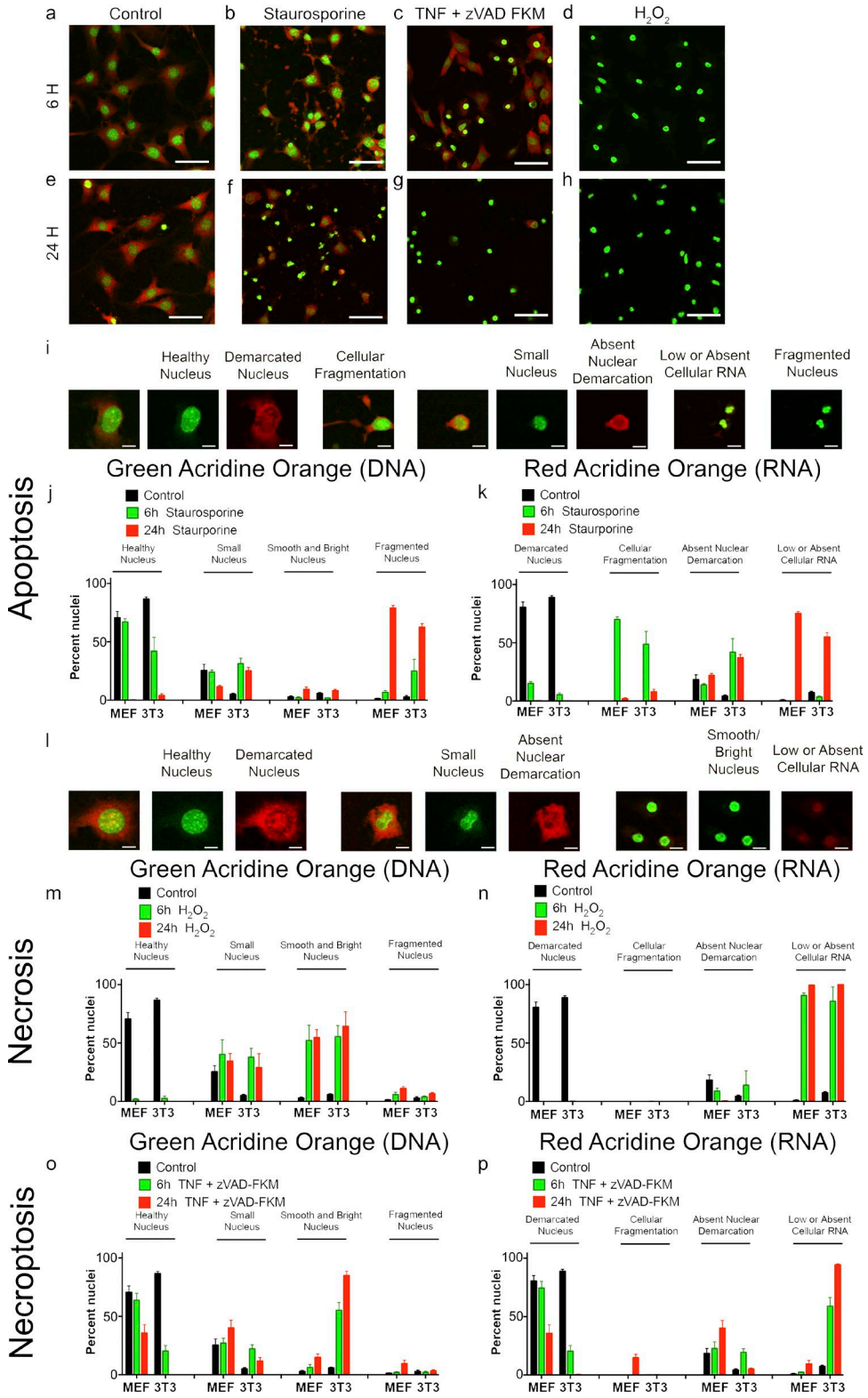

Figure 6. **Apoptosis and necrosis/necroptosis induced distinct morphological features when stained with AO.** (a–h) Representative images of 3T3 NIH cells untreated (a and e) or treated with staurosporine (b and f), TNF/zVAD-FMK (c and g), or H_2O_2 (d and h) for 6 (a–d) or 24 (e–h) h. (j, k, and m–p) Morphology can be segmented in AO cells based on nuclear (green AO emission; j, m, and n) and RNA (red AO emissions; k, n, and p) changes. (i–k) Healthy cells had large, well-demarcated granulated nuclei. Staurosporine-induced apoptosis was characterized initially by nuclear shrinkage and cellular fragmentation. Cells later lost their nuclear demarcation, and ultimately lost red AO emission (cellular RNA), exhibiting a fragmented nucleus. (l–p) During necrosis (m and n) or necroptosis (o and p), cells initially had a shrunken nucleus with absent nuclear demarcation. These cells ultimately lacked cellular RNA and possessed a smooth, shrunken, and bright nucleus. Bars: (a–h) 50 µm; (i and l) 10 µm. Data are shown as mean ± SEM.

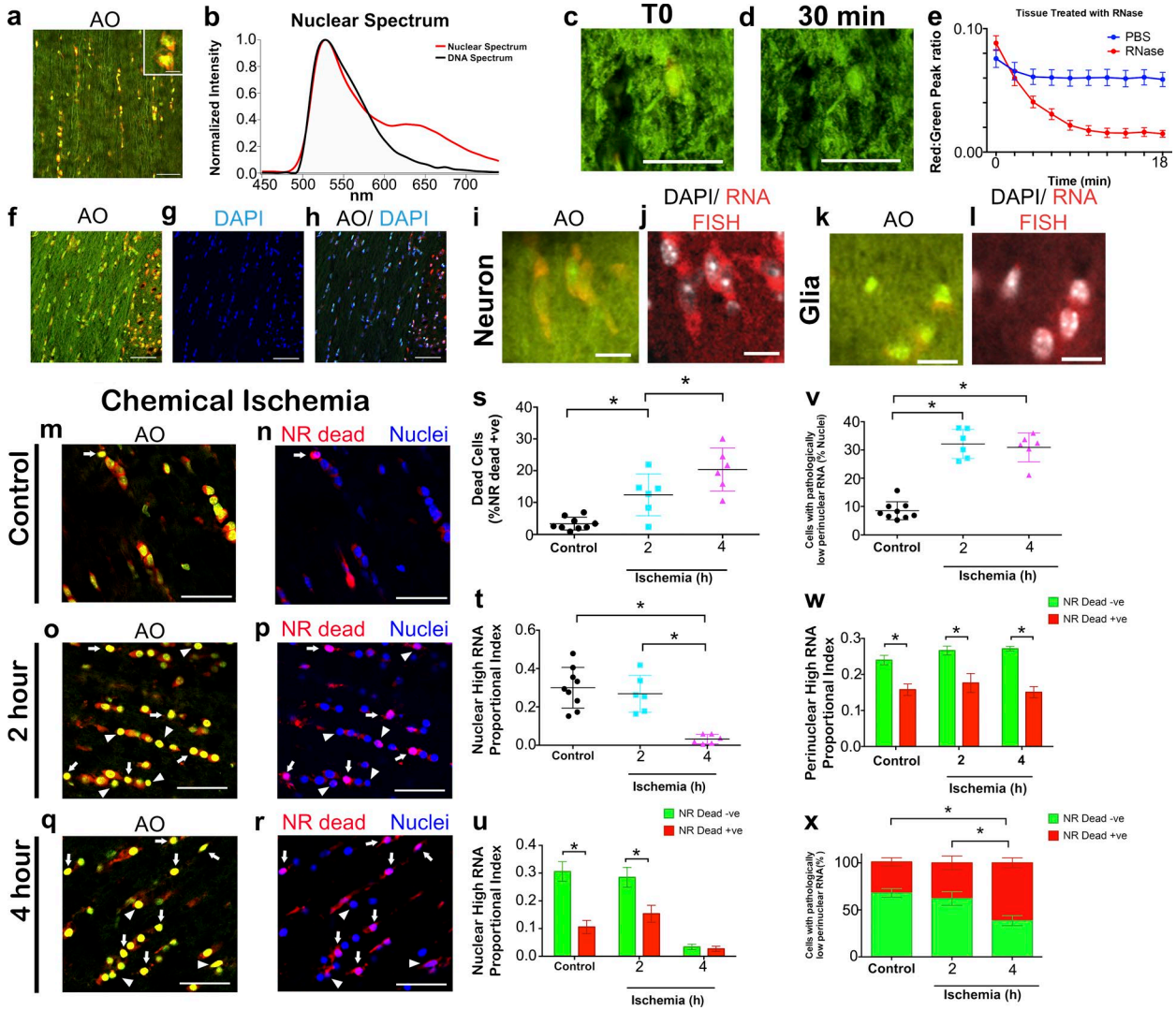

Figure 7. **RNA content and cellular injury can be visualized in fixed tissue stained with AO.** (a and b) AO-stained Thy1-YFP mouse optic nerve showing green axons containing distinct nuclear green and red emission spectra. (c–e) Red emission is RNase sensitive. (f–h) Green AO emissions colabeled with the nuclear probe DAPI. (i–l) In the mouse spinal cord, red AO emission colabeled with *gapdh* RNA in neurons (i and j) and glia (k and l). (m–r) In mouse optic nerves, RNA/red AO emission decreased with chemical ischemia. Optic nerves were incubated with a normally cell-impermeant nuclear dye, NR Dead. Loss of nuclear and cytoplasmic AO red emission (m, o, and q) coincided with an increase in NR Dead$^+$ cells (n, p, and r) compared with untreated control optic nerves (arrows indicate NR Dead$^+$/AO$^{\text{low perinuclear red}}$ cells, whereas arrowheads show those that are NR Dead$^-$/AO$^{\text{low perinuclear red}}$, indicating that lack of red AO signal identifies both injured and dead cells). (s) Chemical ischemia induced a significant increase in NR Dead$^+$ cells. (t) Chemical ischemia resulted in a decrease in the proportional index of high-RNA (low index) kernels within the nucleus. (u) Comparing within NR Dead$^+$ and NR Dead$^-$ cells, the decrease in the nuclear high-RNA proportional index did not always differ between NR Dead$^+$ and NR Dead$^-$ cells. (v) There was an increase in the number of AO$^{\text{low perinuclear red}}$ cells at 2 and 4 h after chemical ischemia compared with control optic nerves. (w) Quantitative assessment of high RNA indexes demonstrates a decreased perinuclear proportional index for NR Dead$^+$ cells compared with NR Dead$^-$ cells, irrespective of whether it was from aCSF-treated control nerves or 2 or 4 h of ischemia. (x) The proportion of AO$^{\text{low perinuclear red}}$ cells that were NR Dead$^+$ increased over the course of chemical ischemia. Collectively, both nuclear and perinuclear loss of red AO emission occurs after ischemia, but the decrease in perinuclear red AO signal is more sensitive to cell membrane permeability. Bars: (a, f–h, and m–r) 50 µm; (c and d) 20 µm; (i–l and a [inset]) 10 µm. Data are shown as mean ± SEM. *n* = 8, 6, and 6 for control, 2-h, and 4-h chemical ischemia, respectively (*n* is a single optic nerve). Data were analyzed with two-way ANOVA using Sidak's multiple comparison test.

signal with RNA FISH directed toward *GAPDH* (Fig. 7, f–l). Collectively, common tissue-processing techniques adequately preserve cellular RNA, which can be measured along with DNA changes based on the AO spectrum.

To define the relationship between RNA loss and cellular injury in a model that induces widespread damage and necrosis, we isolated optic nerves and induced chemical ischemia ex vivo with the oxidative phosphorylation blocker, sodium azide, and the glycolytic inhibitor, iodoacetate. Tissue was incubated with NucRed Dead 647 (NR Dead), a PI-like agent used to determine whether cell membranes have been compromised by necrosis. Chemical ischemia in mouse optic nerves induced a significant loss of red AO signal in both the nucleus and cytoplasm (Fig. 7, m–r), which was associated with a progressive increase in the density of NR Dead–positive cells over time (Fig. 7 s). However, the decrease in nuclear red AO emission was altered in a similar manner irrespective of whether the cellular membrane was compromised after chemical ischemia, suggesting that it was sensitive to ischemic damage but not as responsive to cell membrane permeability (Fig. 7, t and u). By comparison, cy-

toplasmic loss of red AO emission (i.e., AO$^{low\ perinuclear\ red}$ cells) increased at 2 and 4 h after chemical ischemia (Fig. 7 v), and analysis of cytoplasmic red AO emission demonstrated that there was less perinuclear red AO signal in NR Dead^{+} cells even at the earliest ischemic time point (Fig. 7, w and x). This indicates that loss of cellular red AO emission—and hence RNA—decreased within cells as their cellular membrane became permeable. Indeed, almost all NR Dead^{+} cells (97%) lacked perinuclear red AO emission. The loss of cytoplasmic red AO signal preceded cell membrane permeability (Fig. 7 x), indicating that this feature is an early marker of cell injury/death. Interestingly, the morphological features of AO$^{low\ perinuclear\ red}$ cells was similar to necrosis/necroptosis in culture (Fig. 6), with a bright smooth nucleus having little to no perinuclear red AO emissions. Thus, this might represent a more general feature of necrosis useful for distinguishing cells undergoing this mechanism of cell death. Collectively, the loss of perinuclear RNA, readily detected by the AO spectral method, was an early pathological indication of injury in cells that preceded membrane permeability under ischemic conditions.

We next examined RNA changes in an in vivo model of white matter injury that is known to induce apoptosis. Dietary consumption of the copper chelator cuprizone (CPZ) induces reproducible oligodendrocyte apoptosis and demyelination of the corpus callosum, a major white matter tract in the brain. Oligodendrocyte apoptosis peaks 2–4 wk after the start of CPZ consumption, with demyelination maximal at 4 wk (Ludwin, 1978; Mason et al., 2000a,b; Matsushima and Morell, 2001). To determine whether the AO method could reliably represent CPZ-induced cellular injury, brain sections were collected from mice after 2 wk of CPZ diet and stained with AO. Although at this time point there was no overt demyelination of the corpus callosum (Fig. 8, a–c), there were numerous cells devoid of perinuclear red AO emission indicative of cellular injury/death, which was not seen in controls fed standard diet (Fig. 8, d and e, and Fig. 9, a–c). Quantitative analysis demonstrated that in CPZ-fed mice, there was a significant decrease in perinuclear red AO signal (Fig. 8, f–h). Those AO$^{low\ perinuclear\ red}$ cells colabeled with the oligodendrocyte specific marker, myelin-associated glycoprotein (MAG), and the oligodendrocyte lineage marker, olig2 (Fig. S5), consistent with studies of oligodendrocyte death in this model. AO$^{low\ perinuclear\ red}$ cells also colabeled with the classic apoptosis markers TUNEL and cleaved caspase 3 (CC3; Fig. 8, i–m, and Fig. 9, d–h). However, unlike NR Dead^{+} cells observed after chemical ischemia, the apoptotic cells could be classified into two categories: (a) strong nuclear red AO emission or (b) fragmented nuclear green emission (Fig. 9, d–h). Therefore, apoptotic cells and NR Dead^{+} cells possess distinct AO spectral properties. Indeed, the vast majority of AO$^{low\ perinuclear\ red}$ cells from CPZ-fed mice (Fig. 8 m, black bars) failed to colabel with apoptotic markers (Fig. 8, i–m). Instead, these cells possessed the round bright nucleus observed in necrotic/necroptotic cells, suggesting they might be either highly injured or, based on morphological observations in culture and ex vivo, undergoing necrosis/necroptosis. The observation of necroptosis in this model is consistent with the work of others (Ofengeim et al., 2015). Collectively, AO spectral changes in fixed tissue provided a reliable signature for injured cells, with morphological staining features that are distinct between necrotic/necroptotic and apoptotic mechanisms of cell death.

Pathological changes of AO spectra were not restricted to chemical ischemia and CPZ injury. Injection of LPC into white matter is a well-described model to induce myelin loss that is associated with prominent depletion of oligodendrocytes and their progenitors within 48 h (Hall, 1972; Hinks and Franklin, 1999; Fancy et al., 2004). LPC injection into ventral columns of mouse spinal cord induced a profound loss of cytoplasmic RNA from cells within the lesion site, peaking 4 and 24 h after injection, together with a significant decrease in nuclear AO red emission at 4 and 8 h (Fig. 10, a–i). This recovery by 24 h could reflect a rapid influx of immune cells known to occur quickly after such injury (Ousman and David, 2000, 2001), but also might represent cellular recovery. Collectively, these data suggest that LPC toxicity is associated with decreased nuclear and cytoplasmic RNA.

Pathological changes of AO spectra were also informative after trauma. Spinal cord injury (SCI) results in early necrosis at the lesion epicenter and widespread oligodendrocyte apoptosis in the ensuing weeks (Crowe et al., 1997; Plemel et al., 2014). In agreement, we also found many nuclei lacking cytoplasmic red AO emission, suggesting cellular injury. Early after injury, necrotic cells are present in the lesion site (Liu et al., 1997). 3 d after SCI, cells lacking cytoplasmic red AO signal were found within and adjacent to the lesion site (Fig. 10, j and k). By 3 wk after SCI, oligodendrocyte apoptosis was still ongoing, often at large distances from the lesion epicenter (Crowe et al., 1997). We found that by 28 d after injury, within the spared tissue adjacent to the lesion site, there were still cells lacking cytoplasmic red AO emission with round and bright nuclei (Fig. 10, l and m). This suggests ongoing cellular injury and perhaps necrosis 28 d after SCI. Collectively, our spectral AO method reliably reported a loss of cellular RNA and cellular injury in a broad array of central nervous system white matter pathologies. The morphological attributes of AO that are suggestive of necrosis/necroptosis also provide evidence that these mechanisms of cell death are much more common than previously appreciated.

Discussion

The fluorescence spectrum of AO is a powerful tool to measure changes in cells undergoing injury. One advantage of AO staining over many other techniques is that AO is useful in fixed tissues and cells, and thus is compatible with conventional pathological samples, for which there are few tools available. At the concentrations used here, AO exhibits a spectrum that contains a distinct red emission peak after interacting with RNA. We found that this red AO signal strongly correlates with RNA and is therefore a useful proxy for measuring RNA signatures after various insults. These analyses yielded spectral and morphological properties that are indicative of injury. Based on chemical ischemia in the optic nerve and corroborating cell culture studies, the early signs of necrosis/necroptosis include a decrease in the relative amount of nuclear red emission of AO and a shrinkage of general cellular structures, reflecting a loss of cellular RNA. As cells proceed to die, they further lose cytoplasmic RNA; this feature preceded membrane permeability changes or necrosis, further underscoring the sensitivity of the AO method to very early cell injury. Necrotic/necroptotic cells are characterized as those completely lacking cellular RNA but having a round, bright nucleus. In contrast, apoptotic cells also lose cytoplasmic RNA, but in vivo these cells had unique AO emissions: the nucleus contained either red or fragmented green emission. These features were never observed in necrotic cells. Thus, changes in AO spectrum differed with respect to necrosis/necroptosis versus apoptosis, underscoring the ability of this probe to reliably distinguish modes of injury.

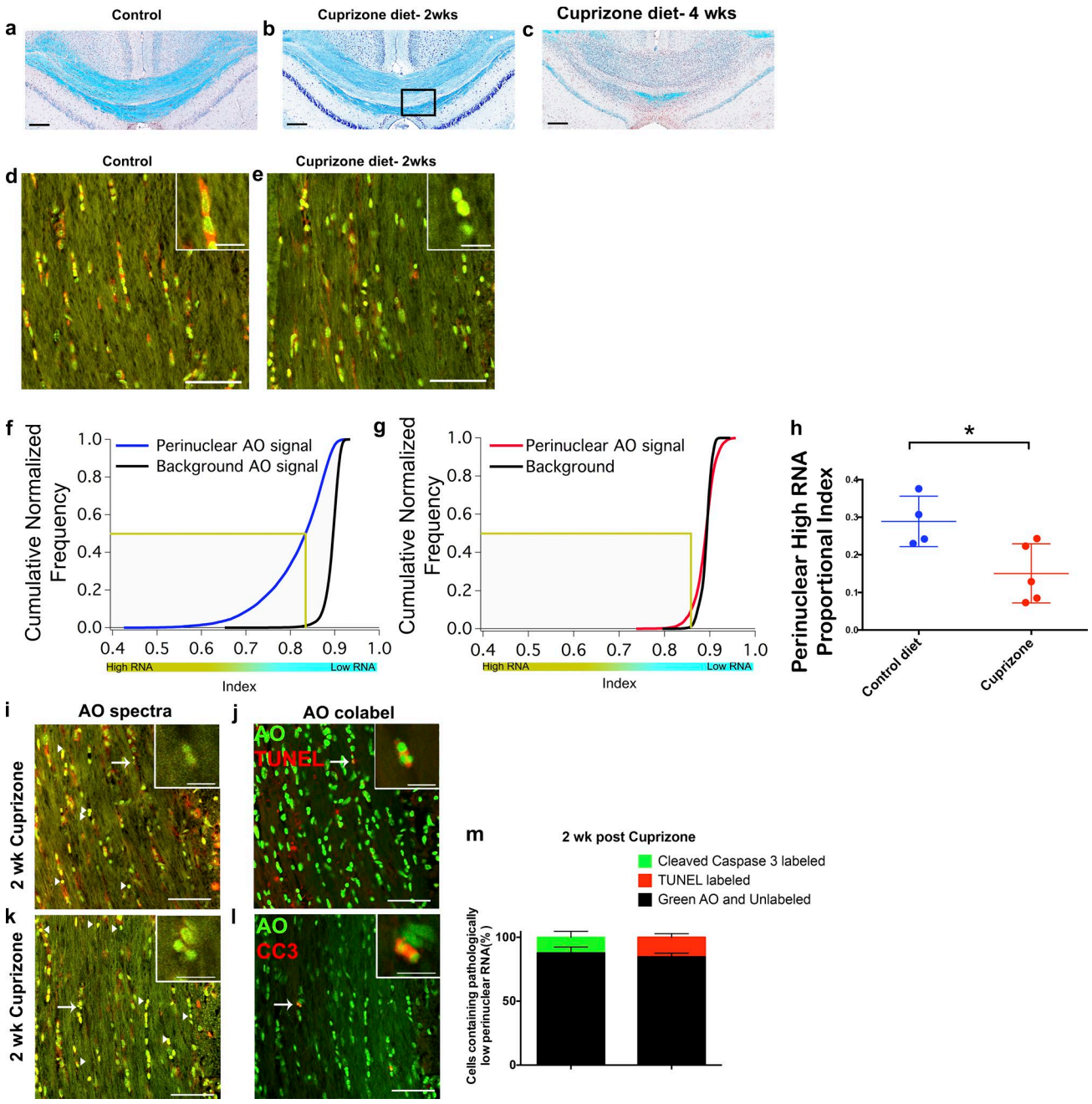

Figure 8. **In tissue sections from CPZ-fed mice, AO spectral properties identify more subtle pathology than standard techniques.** (a–c) CPZ feeding induced prominent demyelination of the corpus callosum (blue LFB), but only after 4 wk (c). Box in b specifies representative region imaged with spectral confocal microscopy, except with orthogonal orientation (d, e, and i–l). After 2 wk of dietary CPZ, despite preservation of myelin, there is prominent loss of perinuclear red AO emission in callosal cells from CPZ mice compared with controls, suggesting a decrease in cellular RNA (d and e; image is oriented along medial to lateral axis). (f–h) After 2 wk of CPZ, there is a significant loss of perinuclear red AO emission as seen in cumulative normalized frequency histograms. (f and g) The perinuclear or background kernels are presented as a cumulative normalized frequency histogram. (h) The kernels enclosed by gold boxes (those with lower indexes than all but 1% of background) were quantified and are presented as the proportional index (mean index of those kernels as a proportion of all kernels measured). (i–m) Cells colabeled with classic apoptosis markers, TUNEL, or CC3 comprise a small minority of the $AO^{low\ perinuclear\ red}$ cells. AO therefore identified early injury undetected by conventional techniques. Arrowheads indicate $AO^{low\ perinuclear\ red}$ cells that are $TUNEL^{-}$, whereas arrows indicate $TUNEL^{+}$ cells. Bars: (d, e, and i–l) 50 µm; (inset) 10 µm; (a–c) 100 µm. Data are shown as mean ± SEM. $n = 4$ for control mice and $n = 5$ for CPZ-fed mice. Data were analyzed with Student's *t* test.

Necrosis in white matter injury

One surprising observation from this study was a high proportion of cells with a bright green nucleus lacking red AO signal, or $AO^{low\ perinuclear\ red}$ cells, in several conditions of white matter injury. Fibroblast cells in culture that have these features are those treated with either necrotic or necroptotic stimuli. Indeed, few cells undergoing apoptosis possessed smooth and bright green nuclei, suggesting that this feature is not a prominent intermediate stage during apoptosis. These $AO^{low\ perinuclear\ red}$ cells were commonly located in the ischemic optic nerve, a treatment known to induce necrosis/necroptosis (Fern, 1998), again suggesting that $AO^{low\ perinuclear\ red}$ cells are a reliable indicator of

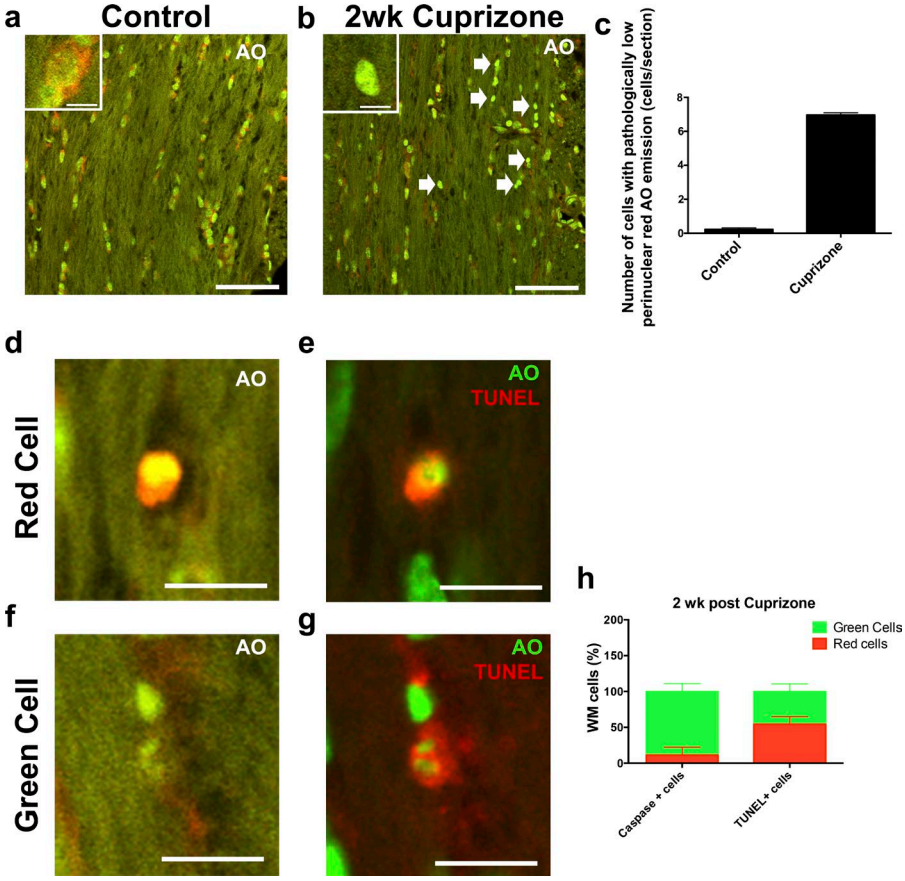

Figure 9. **CPZ caused injury reflected by increased density of cells lacking red AO emission.** (a–c) Control mouse corpus callosum (a) had prominent red AO emission (i.e., RNA-rich) around the vast majority of nuclei, whereas CPZ-fed mice (b) contained ∼35× more nuclei lacking this cytoplasmic red AO emission (arrows), as quantified in c. (d–g) AO sections were imaged and then stained with classic apoptosis markers such as TUNEL or anti-CC3 before reimaging. Micrographs were acquired from the corpus callosum after AO staining (d and f) or TUNEL staining (e and g; red). (h) Nuclei that expressed apoptotic markers TUNEL or CC3 could be categorized as either having a high red AO spectrum within the nucleus ("red cells"; d) or lacking apparent red AO emission ("green cells"; f). The green cells were often fragmented, suggesting that they are cells from a later stage of apoptosis. Collectively, early and late apoptotic cells have a distinct AO signature. As nuclei undergo apoptosis, they first appear as red cells and later progress into green cells when stained with AO. Bars: (a and b) 50 µm; (d–g) 10 µm; (insets a and b) 5 µm. Data are shown as mean ± SEM. (c) $n = 4$ and 6 for control and CPZ, respectively. (h) $n = 3$. (c) Data analyzed with unpaired t test.

necrosis/necroptosis. Because these AO$^{\text{low perinuclear red}}$ cells are observed before cell membrane permeability, they might also be prenecrotic/necroptotic. However, based on data from our studies in culture and ex vivo, the presence of AO$^{\text{low perinuclear red}}$ cells precedes cell membrane permeability by only a few hours to a day. Therefore, AO$^{\text{low perinuclear red}}$ cells are likely cells with severe metabolic dysfunction that have lost cytoplasmic RNA and are in the process of undergoing necrosis/necroptosis.

These AO$^{\text{low perinuclear red}}$ cells are present in abundance after 2 wk of CPZ consumption, a time point that was chosen because it lacks overt myelin pathology. Animals on the CPZ diet contain apoptotic cells in the corpus callosum for 2–4 wk, with the peak of apoptosis occurring 3 wk after CPZ treatment (Matsushima and Morell, 2001). The amount of AO$^{\text{low perinuclear red}}$ cells in our study exceeded apoptotic cells by almost 10-fold at a time when apoptosis is reported to begin, suggesting that necrosis/necroptosis precedes and/or exceeds apoptosis in the post-CPZ period. Therefore, although apoptosis is the mode of cell death most commonly cited in this model, our data suggest that necrosis/necroptosis predominates. The causes of initial cell death in the CPZ model are unknown, but CPZ is thought to impair oligodendrocyte mitochondrial function and induce oxidative stress, which ultimately culminate in oligodendrocyte demise (Matsushima and Morell, 2001; Kipp et al., 2009; Liu et al., 2010). Our data here, collected based on AO emissions, would predict that oxidative stress in the CPZ model—much like H_2O_2 in cultured cells—drives necrotic cell death.

Another important model of white matter injury is accomplished by injecting the neurotoxic agent LPC into the brain or spinal cord. Previously, there has been scant data describing how cells are injured by LPC, but in our study we observed lesion sites containing predominantly AO$^{\text{low perinuclear red}}$ cells, indicative of necrosis/necroptosis. Previously, it was not possible to visualize these necrotic cells after LPC injection because current proapoptotic tools do not capture this form of cell death. However, using AO staining, it was possible to readily measure cellular injury induced by LPC toxicity. We find using AO staining that the peak in cell death after LPC injections is rapid, 4–8 h after injection.

Cell death after SCI is known to occur in the weeks after trauma (Crowe et al., 1997; Liu et al., 1997; Abe et al., 1999), but previously this was determined using proapoptotic markers such as TUNEL staining, nuclear fragmentation (Crowe et al., 1997; Liu et al., 1997; Emery et al., 1998; Abe et al., 1999), and DNA laddering on gel electrophoresis (Casha et al., 2001). Necrosis after SCI was thought to be confined to the acute periods after injury (Liu et al., 1997; Grossman et al., 2001). Here, we extend these findings using AO staining and find the presence of AO$^{\text{low perinuclear red}}$ cells even 28 d after SCI. Because this pattern represents cells undergoing necrosis/necroptosis, our technique now allows us to extend our understanding of the time course and type of cellular injury after spinal cord trauma, indicating that necrosis/necroptosis is not restricted to the acute phase but also occurs in the weeks after injury.

Distinguishing between apoptosis and necrosis/necroptosis

In vitro, all mechanisms of cell death induced a loss of RNA, but the morphological appearances of this RNA loss were different: based on red AO signal, apoptotic cells had a fragmentation of cellular structures, whereas necrotic/necroptotic cells

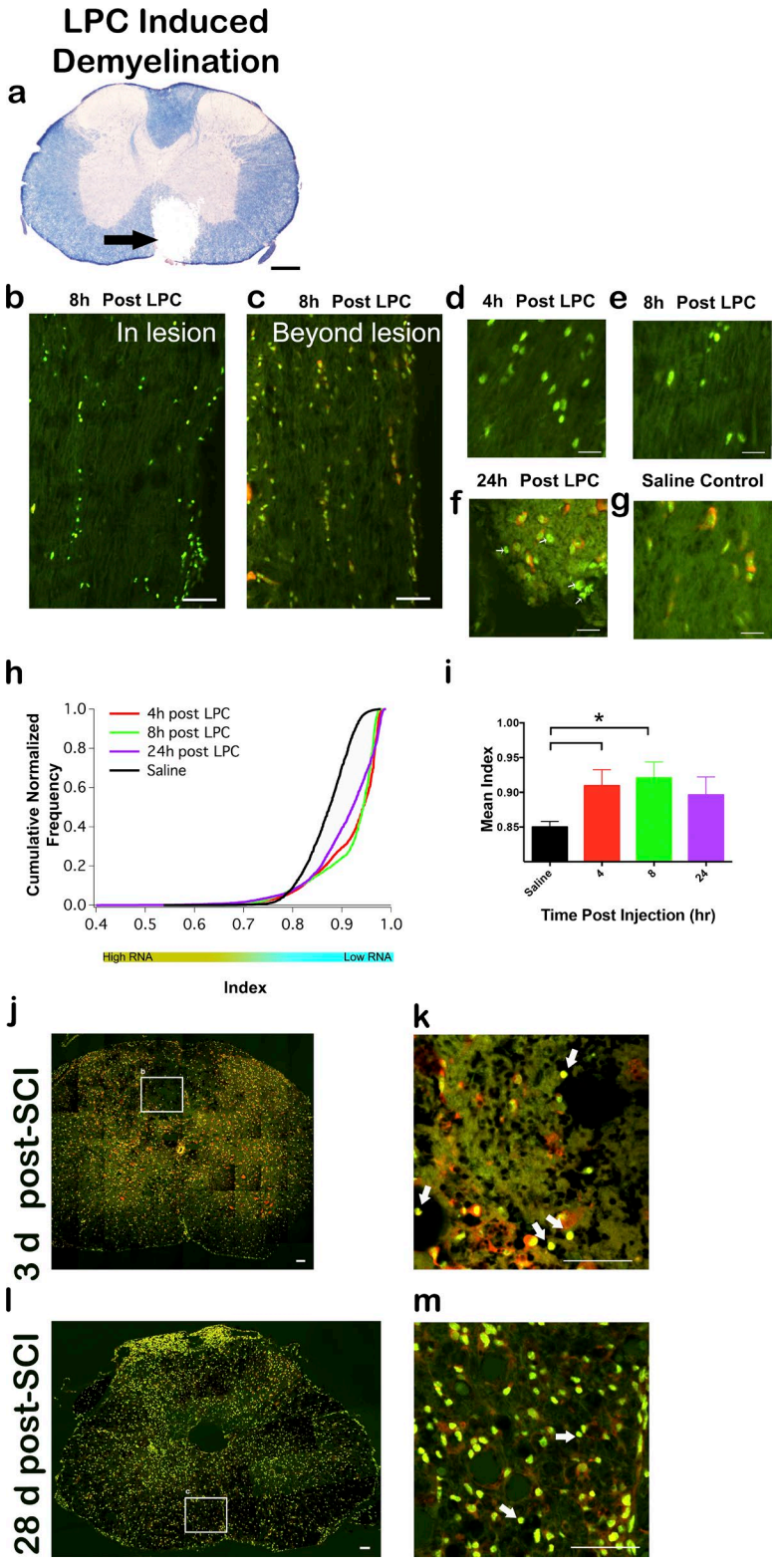

Figure 10. **Loss of cellular red AO emission (i.e., RNA) after LPC-induced demyelination or traumatic SCI.** (a) LPC was injected into the ventral spinal cord white matter (arrow). (b and c) Lesions had lower nuclear and cytoplasmic RNA (i.e., less red emission). (d–g) Representative AO-stained sections taken at 4 (d), 8 (e), and 24 (f) h postinjection compared with saline-injected control (g). Nuclei within the lesion epicenter lacked cytoplasmic red AO emission; this was extensive as early as 4 h after LPC injection (d), but there were also cells lacking cytoplasmic RNA at 24 h after LPC (f; arrows). (h) Analysis displayed using a cumulative normalized frequency histogram of nuclear kernels demonstrates a rightward shift toward higher indexes indicative of lower RNA values and greater cellular injury. (i) At 4 and 8 h after LPC injection, there was a significant decrease in mean index. At 3 d after SCI, we found within and adjacent to the lesion site the presence of cells lacking cytoplasmic red AO emission (i.e., reduced RNA; arrows) using spectral confocal microscopy (j and k); this phenotype is indicative of cellular injury or necrosis. (l and m) By 28 d after injury, there are still cells lacking cytoplasmic red AO emission (i.e., reduced RNA; arrows) primarily within the spared tissue adjacent to the lesion site (m). Collectively, AO spectral phenotyping can measure cellular injury after SCI- and LPC-mediated demyelination. Bars: (a) 200 µm; (c, d, l, and m) 50 µm; (d–g) 10 µm. Data are shown as mean ± SEM. n = 8, 4, 3, and 4 for control, 4, 8, and 24 h after LPC, respectively.

had early loss of nuclear demarcation followed very quickly by a near-complete loss of red AO signal. Ultimately, both apoptotic and necrotic/necroptotic cells lost red AO signal. The most defining distinction between apoptosis and necrotic/necroptotic cells was that apoptotic cells lost red AO signal but at the same time had nuclear fragmentation. In contrast, necrotic/necroptotic cells had a smooth and often bright nucleus while still lacking red AO signal.

In tissue, the distinctions between apoptosis and necrosis/necroptosis using AO staining were similar. Here, early apoptosis was characterized by a red AO signal within the nucleus, which was followed by nuclear fragmentation. The character-

ization of cells with a permeabilized membrane (i.e., necrotic cells) in tissue appeared identical to that of in vitro necrotic/necroptotic cells: they lacked red AO signal but displayed a smooth and often bright nucleus.

RNA loss induced by different mechanisms

Loss of cellular RNA is an early and general feature of cellular injury. There are two possible reasons. First, RNA degradation might be triggered in an active manner as a component of cell injury/death (Cidlowski, 1982; King et al., 2000; Del Prete et al., 2002). We found that after staurosporine treatment, cells maintained high energy levels and did not contain signs of RNA integrity loss until cellular membranes became permeable. These data are all consistent with an active, concerted degradation of RNA (Mondino and Jenkins, 1995; Del Prete et al., 2002; Bushell et al., 2004; Padmanabhan et al., 2012). Second, cellular RNA levels might reflect cellular metabolism. RNases are ubiquitous in all cells of the central nervous system (Zhang et al., 2014), and RNA decay is an ongoing process of cellular function (Schoenberg and Maquat, 2012). As RNA production requires energy (Wagner, 2005) and there is constant RNA decay within the cell, overall RNA levels might thus be a proxy for cellular metabolism. We found that cells treated with H_2O_2, which induces necrosis at the levels used, lost cellular energy before RNA degradation. Thus, necrotic cell death might result in RNA loss caused by an overall failure in cellular metabolism. This RNA loss in combination with poor DNA fragmentation—a characteristic necrosis marker (Krysko et al., 2008)—is one possible explanation as to why necrotic/necroptotic cells lose cellular RNA but maintain an unfragmented nucleus.

Conclusion

Reliable and sensitive methods that inform on cellular injury preceding death are lacking for fixed cells and tissue sections. AO spectroscopy, as outlined here, provides a new, sensitive, quantitative, and unbiased method to image cellular RNA, which in turn reflects early cellular injury not readily observed using traditional cell injury markers. Such a tool is highly desirable, as more subtle damage may contribute to brain dysfunction in various diseases. This strategy also captures cell death through different mechanisms, such as apoptosis versus necrosis versus necroptosis, and might serve to uncover new forms of cell damage.

Materials and methods

Animals

Nine C57/Bl6 (CPZ experiments) and 33 Thy1-YFP (chemical ischemia and LPC experiments) mice were used in this study. All animal experiments were conducted in accordance with procedures reviewed and approved by animal subcommittees at the University of Calgary.

Spectral confocal microscopy

All spectral images were captured using a custom modified microscope (A1R or C1si; Nikon) equipped with a spectral detector allowing a one-shot acquisition of a given spectral range with a multi-anode photomultiplier tube capable of capturing 32 spectral bins. Spectral images were typically acquired with 10-nm resolution covering the range of 430 to 750 nm. The C1si was equipped with a 10× Air lens (NA 0.45, Plan Apo; Nikon), and images were acquired using EZ-C1 software (Nikon). The A1R was equipped with a 25× lens (NA 1.1, Apo LWD; Nikon) with water or PBS as an imaging medium, and images were acquired using NIS Elements (Nikon). Images were imported into ImageTrak (written by P.K. Stys; see Image analysis); emission spectra were determined within a given region of interest using ImageTrak.

Spectral properties of DNA, RNA, and BSA

AO of various concentrations was mixed with DNA (250 ng/µl; isolated with DNeasy; QIAGEN) and RNA (140 ng/µl; isolated with RNeasy; QIAGEN) isolated from cell cultures and 1 mg/ml BSA. Solutions were imaged by drawing solutions into capillary tubes, which could then be imaged with a water dipping lens. Images were all collected using 457-nm excitation with the Nikon A1 spectral confocal microscope.

Cell culture

MO3.3 cells. Human glial (oligodendrocytic) hybrid cell line MO3.13 (#CLU301; Cedarlane) were expanded in high-glucose DMEM (Thermo Fisher Scientific) supplemented with 1 mM sodium pyruvate, 2 mM L-glutamine or 1× GlutaMAX, 50 U/ml penicillin, 50 µg/ml streptomycin, and 10% FBS (Thermo Fisher Scientific) on 100-mm tissue culture plates (Corning). For experiments, MO3.13 cells were plated at 5,000 cells per well in 96-well tissue culture plates (Corning) with high-glucose DMEM containing 1 mM sodium pyruvate, 2 mM L-glutamine or 1× GlutaMAX, 50 U/ml penicillin, 50 µg/ml streptomycin (Thermo Fisher Scientific), and 100 nM PMA (EMD Millipore). MO3.13 cells were plated 48–72 h before toxicity experimentation. To measure RNA, ATP, and LDH release in comparison to red AO emission, 1.0×10^5 MO3.13 cells were plated on six-well tissue culture plates. RNA was isolated by lysing cells in TRIzol (Thermo Fisher Scientific), adding chloroform, and, after 11,500 rpm centrifugation, collecting the aqueous phase. Ethanol (70%) was added to this aqueous phase, and the resulting solution was added to RNeasy isolation columns (QIAGEN). From this point, RNA was isolated following the manufacturer's instructions. RNA integrity was measured by the University of Calgary Genomics and University Core DNA Services using Agilent TapeStation 2200. ATP was measured from cell lysates using the CellTiter-Glo Luminescent Cell Viability Assay, and LDH release was measured using the CytoTox-ONE Homogenous Membrane Integrity Assay (Promega). For LDH, ATP, and RNA measurements, data are presented as the percentage of the mean control for each experimental time point and experimental group.

Oligodendrocyte cultures. Mice (CD-1) cortices of P1/2 pups were isolated, diced, and digested in a solution containing papain (1.54 µg/ml; Worthington), L-cysteine (360 µg/ml; Sigma-Aldrich), and DNaseI (703 µg/ml; Roche) for 25 min at 37°C as outlined previously (O'Meara et al., 2011). Dissociated cells were plated at high density on T75 tissue culture flasks coated with poly-L-lysine (PLL; Sigma-Aldrich) for 7–10 d in high-glucose DMEM supplemented with 1 mM sodium pyruvate, 2 mM L-glutamine or 1× GlutaMAX, 50 U/ml penicillin, 50 µg/ml streptomycin, and 10% FBS. Confluent T75 flasks were shaken overnight 18–20 h at 220 rpm, and the supernatant was incubated for 30 min on a tissue culture plate to remove adherent cells. Nonadherent cells were plated at 5,000 cells per well in PLL-coated 96-well tissue culture plates in oligodendrocyte growth medium composed of high-glucose DMEM supplemented with 1 mM sodium pyruvate, 1× GlutaMAX, 50 U/ml penicillin, 50 µg/ml streptomycin, 1× B27 supplement (Thermo Fisher Scientific), 50 µg/ml holo-transferrin, 100 µg/ml albumin from bovine serum, 5 ng/ml sodium selenite, 16 µg/ml putrescine, 60 ng/ml progesterone, 400 ng/ml 3,3′,5-thiiodo-L-thryonine, 5 µg/ml bovine insulin, 5 µg/ml *N*-acetyl cysteine, 10 ng/ml D-biotin (Sigma-Aldrich), and 1× Trace Elements B (Corning). After 24 h in vitro, cells were treated with toxins for a defined period of time.

Ex vivo chemical ischemia of mouse optic nerves

Optic nerves were carefully dissected from Thy1-YFP mice (6–8 wk old) and placed on ice in artificial cerebrospinal fluid (aCSF) buffer solution containing 126 mM NaCl, 3 mM KCl, 2 mM $CaCl_2$, 1.25 mM NaH_2PO_4, 26 mM $NaHCO_3$, 2 mM $MgSO_4$, 2 µM copper sulfate, and 10 mM D-glucose, bubbled with 95% O_2/5% CO_2 to maintain pH 7.4 as previously described (Micu et al., 2007). Optic nerves were incubated with NR Dead (Thermo Fisher Scientific) as per the vendor's instructions. To induce chemical ischemia, nerves were incubated with 2 mM sodium azide and 1 mM iodoacetate. At specified time points, nerves were washed 3× in aCSF and fixed with 4% PFA overnight. Nerves were cryoprotected in 30% sucrose, cryosectioned, stained with 50 µM AO, and imaged using a Nikon A1 spectral confocal microscope. Images were captured and quantified by a blinded observer.

LPC surgery

Focal demyelination was produced in the ventral spinal cord white matter by injection of the detergent lysolecithin (Keough et al., 2015). In brief, mice (Thy1-YFP, 8–12 wk old) were anesthetized with a mixture of ketamine and xylazine. The spinal cord was surgically exposed by removing the connective tissue between T3 and T4 vertebrae. After removing the dura with a 32-gauge metal needle, the spinal cord was pierced just lateral of the midline with a prepulled glass capillary attached to a 10-µl syringe at a depth of 1.3 mm. A 0.5-µl volume of 1% lysolecithin containing NucBlue (Thermo Fisher Scientific) in PBS was deposited over 2 min, and the capillary was kept in place for another 2 min to prevent backflow. Control surgeries were performed identically, with an injection of PBS alone. The capillary was then slowly withdrawn, and the overlying musculature and skin were closed with sutures. Postoperative buprenorphine was administered as an analgesic, and the mice were kept in a heated recovery chamber until they became ambulatory and were returned to their cages until the time of death. Mice were killed via transcardial perfusion. Tissue was collected and fixed overnight with 4% PFA before cryoprotecting in a high-sucrose solution, freezing, cryosectioning, staining with 50 µM AO, and imaging using an A1 spectral confocal microscope. Images were captured and quantified by a blinded observer.

CPZ treatment

Male C57BL/6 mice were fed a 0.2% CPZ diet starting at 7–8 wk of age. Standard mouse diet and CPZ powder (C9012; Sigma-Aldrich) were blended together once a week. Mice continued on a CPZ-only diet for 2 wk, at which point they were killed via transcardial perfusion. After overnight fixation with 4% PFA, brains were cryoprotected in a high-sucrose solution, cryosectioned, stained with 50 µM AO, and imaged using a Nikon A1 spectral confocal microscope. Images were captured and quantified by a blinded observer.

Contusion SCI

Spinal cord contusion is a clinically relevant experimental SCI model. In brief, 10-wk-old female C57 mice were anaesthetized with a mixture of 1.5% isoflurane and oxygen. Buprenorphine and enrofloxacin (Baytril) were given before surgery. Under deep anesthesia and aseptic conditions, a 1.5-cm midline incision was made on the back, and laminectomy at T10 was performed to expose the underlying spinal cord. The animal was then impacted with an Infinite Horizon 4000 spinal cord impactor (Precision Systems and Instrumentations) with a force value of 75 kdynes to induce moderate SCI. After the impact, muscles and skin were sutured in layers, and animals were returned to their cages. Buprenorphine and enrofloxacin were given daily for 3 d after surgery. Urinary bladders were voided twice daily until the mice recovered voluntary bladder function. At the end of the survival period, animals were given a lethal dose of sodium pentobarbital. Animals were then perfused intracardially with normal saline followed by 4% PFA in 0.1 M phosphate buffer, pH 7.4. A segment ±2 mm from lesion epicenter was harvested, postfixed with fresh fixative overnight, and placed in 30% sucrose. Spinal cords were then frozen, cryosectioned, and mounted on precoated slides.

Immunocytochemistry and cellular imaging

Cells in 96-well tissue culture plates were treated with various concentrations of H_2O_2 (Sigma-Aldrich), LPC (Sigma-Aldrich), staurosporine (Sigma-Aldrich), and rotenone (Tocris) for defined periods of time before they were fixed for 10–12 min in 4% PFA and washed 2× in PBS. For staining, cells were incubated with 200 µM AO (Thermo Fisher Scientific) for 10 min before 1× wash in PBS treated with RNAsecure (Thermo Fisher Scientific). For immunocytochemistry, cells were incubated with 10% normal goat serum for 20–40 min. To label for immature and mature oligodendrocytes, coverslips were labeled with mouse monoclonal anti-O4 (1:250, MAB1326; R&D Systems) or rabbit polyclonal anti-GFAP (1:1,000, Z0334; Dako). Primary antibodies were incubated overnight followed by 1–2 h using secondary antibodies goat anti–mouse Alexa Fluor 488 and goat anti–rabbit Alexa Fluor 546 (Thermo Fisher Scientific). Nuclei were stained with NucBlue (Thermo Fisher Scientific) or DAPI (Thermo Fisher Scientific). To measure cell death, live cells were labeled with 5 µM calcein AM (Invitrogen) and dead cells with 5 µg/ml PI (Sigma-Aldrich). Nuclei were labeled with NucBlue. Caspase activity was measured by CellEvents Caspase 3/7 green detection reagent (5 µM; Invitrogen). Quantification of immunocytochemistry, caspase activity, and live/dead cells was conducted using the ImageXpress system (Molecular Devices). Images were captured at physiological temperature and elevated CO_2 (during live imaging sessions) throughout each well using systematic sampling. AO-stained cells were excited using a 488-nm argon laser and captured using spectral confocal microscopy. Spectral images were captured using a custom-modified commercial system (Nikon C1si). Images were captured and quantified by a blinded observer.

Tissue AO staining and immunohistochemistry

Tissue was stained with 50 µM AO for 20 min, and the solution was dabbed away before coating the slide with Fluoromount/Plus (Cedarlane) and covering it with a coverslip. Tissue images were collected using a custom-modified commercial spectral confocal microscope using 476-nm excitation (A1R; Nikon). RNA FISH was conducted using Stellaris protocols against a mouse mRNA housekeeping gene, *GAPDH* (Stellaris probe Quasar 670 Dye; LGC Biosearch Technologies). TUNEL labeling was conducted as per the manufacturer's instructions (Click-iT TUNEL Alexa Fluor 647 imaging assay; Thermo Fisher Scientific). For immunohistochemistry, TUNEL and RNA FISH sections were first stained with AO and imaged before subsequent labeling. For immunohistochemistry, tissue was incubated with 10% normal goat serum in a 0.3% Triton-PBS solution for 30–60 min before being incubated overnight with the following primary antibodies in a 0.3% Triton-PBS solution: mouse monoclonal anti-MAG (1:500; EMD Millipore), polyclonal rabbit anti-olig2 (1:200; EMD Millipore), and rabbit polyclonal anti-CC3 (1:1,000; Cell Signaling Technology). Slides were washed in PBS and incubated for 1–2 h with goat anti-rabbit or goat anti-mouse Alexa Fluor 647 antibodies (1:500; Jackson ImmunoResearch Laboratories, Inc.) in a 0.3% Triton-PBS solution. Certain sections were also stained with DAPI. TUNEL, RNA FISH, and immunohistochemistry images were collected using 640-nm excitation with a Nikon A1 spectral confocal microscope.

Image analysis

All confocal images were imported into ImageTrak for analysis. For spectral analysis of AO images, nuclei were selected by either thresh-

olding an equivalent DAPI image as with the CPZ analysis or using a spectrally sensitive masking feature with the nuclear AO spectrum as a reference. In this case, AO labels nuclei with a green spectrum, which when masked consistently outlines the nucleus. Selected nuclei were then automatically traced, and each traced nuclear spectrum was plotted. To measure red AO emissions, a threshold was calculated by a blinded observer based on the red spectrum. The number of pixels selected in this threshold was calculated for each image, and the mean pixel density was normalized to control images. To measure the peak ratio, each nuclear spectrum was determined by dividing amplitudes of the red peak by the green peak. The green peak is defined as the intensity of emitted light captured by the ∼525-nm bin, and the red peak is defined as the mean intensity of emitted light captured by the ∼625- to 645-nm bins. To shift the peak ratio values taken from cells and tissue lacking RNA to zero, peak ratio values are corrected by the peak ratio value calculated from RNase treated RNA-free samples. For index analysis, each 3 × 3–pixel kernel of a spectral image was classified using a linear unmixing algorithm to determine the position of its spectrum between two extreme bracketing basis spectra, which was assigned a single scalar value (index). Bracketing spectra were obtained by finding the most limiting green and red spectra using AO images. Kernels were then charted on cumulative normalized frequency histograms. Normalized cumulative histograms provide a convenient single readout reflecting the index of the mean (e.g., 50% cumulative normalized threshold) or the majority (e.g., 90% cumulative normalized threshold) of image kernels.

Statistics

Statistical significance was determined using one- or two-way analysis of variance (ANOVA) with post hoc testing or Student's *t* test as appropriate, unless otherwise noted (Prism 6.0; GraphPad). Igor software was used for presentation of waveform graphs (WaveMetrics). All data are presented as mean ± SEM.

Online supplemental material

Fig. S1 describes purity and health of oligodendrocyte cultures. Fig. S2 compares nuclear red AO peak signature in cultured oligodendrocytes under pathological conditions. Fig. S3 describes the spectral AO changes in MO3 cells subjected to staurosporine. Fig. S4 compares AO staining to a cellular membrane stain. Fig. S5 examines colabeling of MAG and olig2 of AO-stained control and CPZ tissue.

Acknowledgments

We thank Janet Wang for her technical support as well as the University of Calgary Genomics and University Core DNA Services and the Regeneration Unit in Neurobiology core facilities at the University of Calgary.

This study was supported by operating grants from Canadian Institutes of Health Research (CIHR), Multiple Sclerosis Society of Canada, Alberta Heritage Foundation for Medical Research, and a CRIO Team grant from Alberta Innovates - Health Solutions (AIHS). J.R. Plemel was supported by fellowships from Canadian Institutes of Health Research, T. Chen Fong, Alberta Innovates - Health Solutions, and the Donna Joan Oxford award from the Multiple Sclerosis Society of Canada. A.V. Caprariello was supported by fellowships from Alberta Innovates - Health Solutions and M.B. Keough was supported by fellowships from Alberta Innovates - Health Solutions and the Multiple Sclerosis Society of Canada. P.K. Stys and V.W. Yong are supported by Canada Research Chairs (Tier 1) awards.

The authors declare no competing financial interests.

Author contributions: J.R. Plemel performed all cell culture and ex vivo experiments; J.R. Plemel and A.V. Caprariello performed all imaging; J.R. Plemel, A.V. Caprariello, G.J. Schenk, and R. Klaver performed immunohistochemistry; A.V. Caprariello performed CPZ experiments; M.B. Keough performed LPC surgeries; T.J. Henry conducted RNA FISH and aided in culture analyses; S. Tsutsui and P.K. Stys developed analysis algorithms; J.R. Plemel, A.V. Caprariello, V.W. Yong, and P.K. Stys cowrote the manuscript; M.B. Keough, S. Tsutsui, G.J. Schenk, and R. Klaver reviewed the manuscript; V.W. Yong and P.K. Stys supervised the project. T.H. Chu conducted spinal cord injury experiments.

Submitted: 9 February 2016
Revised: 24 October 2016
Accepted: 12 January 2017

References

Abe, Y., T. Yamamoto, Y. Sugiyama, T. Watanabe, N. Saito, H. Kayama, and T. Kumagai. 1999. Apoptotic cells associated with Wallerian degeneration after experimental spinal cord injury: A possible mechanism of oligodendroglial death. *J. Neurotrauma.* 16:945–952. http://dx.doi.org/10.1089/neu.1999.16.945

Abend, M. 2003. Reasons to reconsider the significance of apoptosis for cancer therapy. *Int. J. Radiat. Biol.* 79:927–941. http://dx.doi.org/10.1080/09553000310001632958

Barnett, M.H., and J.W. Prineas. 2004. Relapsing and remitting multiple sclerosis: Pathology of the newly forming lesion. *Ann. Neurol.* 55:458–468. http://dx.doi.org/10.1002/ana.20016

Barrientos, A., and C.T. Moraes. 1999. Titrating the effects of mitochondrial complex I impairment in the cell physiology. *J. Biol. Chem.* 274:16188–16197. http://dx.doi.org/10.1074/jbc.274.23.16188

Bushell, M., M. Stoneley, P. Sarnow, and A.E. Willis. 2004. Translation inhibition during the induction of apoptosis: RNA or protein degradation? *Biochem. Soc. Trans.* 32:606–610. http://dx.doi.org/10.1042/BST0320606

Casha, S., W.R. Yu, and M.G. Fehlings. 2001. Oligodendroglial apoptosis occurs along degenerating axons and is associated with FAS and p75 expression following spinal cord injury in the rat. *Neuroscience.* 103:203–218. http://dx.doi.org/10.1016/S0306-4522(00)00538-8

Cidlowski, J.A. 1982. Glucocorticoids stimulate ribonucleic acid degradation in isolated rat thymic lymphocytes in vitro. *Endocrinology.* 111:184–190. http://dx.doi.org/10.1210/endo-111-1-184

Crowe, M.J., J.C. Bresnahan, S.L. Shuman, J.N. Masters, and M.S. Beattie. 1997. Apoptosis and delayed degeneration after spinal cord injury in rats and monkeys. *Nat. Med.* 3:73–76. http://dx.doi.org/10.1038/nm0197-73

Degterev, A., Z. Huang, M. Boyce, Y. Li, P. Jagtap, N. Mizushima, G.D. Cuny, T.J. Mitchison, M.A. Moskowitz, and J. Yuan. 2005. Chemical inhibitor of nonapoptotic cell death with therapeutic potential for ischemic brain injury. *Nat. Chem. Biol.* 1:112–119. http://dx.doi.org/10.1038/nchembio711

Del Prete, M.J., M.S. Robles, A. Guáo, C. Martínez-A, M. Izquierdo, and J.A. Garcia-Sanz. 2002. Degradation of cellular mRNA is a general early apoptosis-induced event. *FASEB J.* 16:2003–2005.

Dundr, M. 2012. Nuclear bodies: multifunctional companions of the genome. *Curr. Opin. Cell Biol.* 24:415–422. http://dx.doi.org/10.1016/j.ceb.2012.03.010

Emery, E., P. Aldana, M.B. Bunge, W. Puckett, A. Srinivasan, R.W. Keane, J. Bethea, and A.D. Levi. 1998. Apoptosis after traumatic human spinal cord injury. *J. Neurosurg.* 89:911–920. http://dx.doi.org/10.3171/jns.1998.89.6.0911

Fancy, S.P., C. Zhao, and R.J. Franklin. 2004. Increased expression of Nkx2.2 and Olig2 identifies reactive oligodendrocyte progenitor cells responding to demyelination in the adult CNS. *Mol. Cell. Neurosci.* 27:247–254. http://dx.doi.org/10.1016/j.mcn.2004.06.015

Fern, R. 1998. Intracellular calcium and cell death during ischemia in neonatal rat white matter astrocytes in situ. *J. Neurosci.* 18:7232–7243.

Fragoso, G., A.K. Martínez-Bermúdez, H.-N.N. Liu, A. Khorchid, S. Chemtob, W.E. Mushynski, and G. Almazan. 2004. Developmental differences in HO-induced oligodendrocyte cell death: Role of glutathione, mitogen-activated protein kinases and caspase 3. *J. Neurochem.* 90:392–404. http://dx.doi.org/10.1111/j.1471-4159.2004.02488.x

Frankfurt, O.S., and A. Krishan. 2001. Identification of apoptotic cells by formamide-induced DNA denaturation in condensed chromatin.

J. Histochem. Cytochem. 49:369–378. http://dx.doi.org/10.1177/002215540104900311

Gavrieli, Y., Y. Sherman, and S.A. Ben-Sasson. 1992. Identification of programmed cell death in situ via specific labeling of nuclear DNA fragmentation. *J. Cell Biol.* 119:493–501. http://dx.doi.org/10.1083/jcb.119.3.493

Gown, A.M., and M.C. Willingham. 2002. Improved detection of apoptotic cells in archival paraffin sections: Immunohistochemistry using antibodies to cleaved caspase 3. *J. Histochem. Cytochem.* 50:449–454. http://dx.doi.org/10.1177/002215540205000401

Grossman, S.D., L.J. Rosenberg, and J.R. Wrathall. 2001. Temporal-spatial pattern of acute neuronal and glial loss after spinal cord contusion. *Exp. Neurol.* 168:273–282. http://dx.doi.org/10.1006/exnr.2001.7628

Hall, S.M. 1972. The effect of injections of lysophosphatidyl choline into white matter of the adult mouse spinal cord. *J. Cell Sci.* 10:535–546.

Henderson, A.P., M.H. Barnett, J.D. Parratt, and J.W. Prineas. 2009. Multiple sclerosis: Distribution of inflammatory cells in newly forming lesions. *Ann. Neurol.* 66:739–753. http://dx.doi.org/10.1002/ana.21800

Hinks, G.L., and R.J. Franklin. 1999. Distinctive patterns of PDGF-A, FGF-2, IGF-I, and TGF-beta1 gene expression during remyelination of experimentally-induced spinal cord demyelination. *Mol. Cell. Neurosci.* 14:153–168. http://dx.doi.org/10.1006/mcne.1999.0771

Imbeaud, S., E. Graudens, V. Boulanger, X. Barlet, P. Zaborski, E. Eveno, O. Mueller, A. Schroeder, and C. Auffray. 2005. Towards standardization of RNA quality assessment using user-independent classifiers of microcapillary electrophoresis traces. *Nucleic Acids Res.* 33:e56. http://dx.doi.org/10.1093/nar/gni054

Kapuscinski, J., Z. Darzynkiewicz, and M.R. Melamed. 1982. Luminescence of the solid complexes of acridine orange with RNA. *Cytometry.* 2:201–211. http://dx.doi.org/10.1002/cyto.990020402

Keough, M.B., S.K. Jensen, and V.W. Yong. 2015. Experimental demyelination and remyelination of murine spinal cord by focal injection of lysolecithin. *J. Vis. Exp.* (97); doi:10.3791/52679.

King, K.L., C.M. Jewell, C.D. Bortner, and J.A. Cidlowski. 2000. 28S ribosome degradation in lymphoid cell apoptosis: Evidence for caspase and Bcl-2-dependent and -independent pathways. *Cell Death Differ.* 7:994–1001. http://dx.doi.org/10.1038/sj.cdd.4400731

Kipp, M., T. Clarner, J. Dang, S. Copray, and C. Beyer. 2009. The cuprizone animal model: New insights into an old story. *Acta Neuropathol.* 118:723–736. http://dx.doi.org/10.1007/s00401-009-0591-3

Krysko, D.V., T. Vanden Berghe, K. D'Herde, and P. Vandenabeele. 2008. Apoptosis and necrosis: Detection, discrimination and phagocytosis. *Methods.* 44:205–221. http://dx.doi.org/10.1016/j.ymeth.2007.12.001

Li, N., K. Ragheb, G. Lawler, J. Sturgis, B. Rajwa, J.A. Melendez, and J.P. Robinson. 2003. Mitochondrial complex I inhibitor rotenone induces apoptosis through enhancing mitochondrial reactive oxygen species production. *J. Biol. Chem.* 278:8516–8525. http://dx.doi.org/10.1074/jbc.M210432200

Linkermann, A., and D.R. Green. 2014. Necroptosis. *N. Engl. J. Med.* 370:455–465. http://dx.doi.org/10.1056/NEJMra1310050

Liu, L., A. Belkadi, L. Darnall, T. Hu, C. Drescher, A.C. Cotleur, D. Padovani-Claudio, T. He, K. Choi, T.E. Lane, et al. 2010. CXCR2-positive neutrophils are essential for cuprizone-induced demyelination: Relevance to multiple sclerosis. *Nat. Neurosci.* 13:319–326. http://dx.doi.org/10.1038/nn.2491

Liu, X.Z., X.M. Xu, R. Hu, C. Du, S.X. Zhang, J.W. McDonald, H.X. Dong, Y.J. Wu, G.S. Fan, M.F. Jacquin, et al. 1997. Neuronal and glial apoptosis after traumatic spinal cord injury. *J. Neurosci.* 17:5395–5406.

Löber, G. 1981. The fluorescence of dye-nucleic acid complexes. *J. Lumin.* 22:221–265. http://dx.doi.org/10.1016/0022-2313(81)90022-3

Ludwin, S.K. 1978. Central nervous system demyelination and remyelination in the mouse: An ultrastructural study of cuprizone toxicity. *Lab. Invest.* 39:597–612.

Mao, Y.S., B. Zhang, and D.L. Spector. 2011. Biogenesis and function of nuclear bodies. *Trends Genet.* 27:295–306. http://dx.doi.org/10.1016/j.tig.2011.05.006

Mason, J.L., J.J. Jones, M. Taniike, P. Morell, K. Suzuki, and G.K. Matsushima. 2000a. Mature oligodendrocyte apoptosis precedes IGF-1 production and oligodendrocyte progenitor accumulation and differentiation during demyelination/remyelination. *J. Neurosci. Res.* 61:251–262. http://dx.doi.org/10.1002/1097-4547(20000801)61:3<251::AID-JNR3>3.0.CO;2-W

Mason, J.L., P. Ye, K. Suzuki, A.J. D'Ercole, and G.K. Matsushima. 2000b. Insulin-like growth factor-1 inhibits mature oligodendrocyte apoptosis during primary demyelination. *J. Neurosci.* 20:5703–5708.

Matsushima, G.K., and P. Morell. 2001. The neurotoxicant, cuprizone, as a model to study demyelination and remyelination in the central nervous system. *Brain Pathol.* 11:107–116. http://dx.doi.org/10.1111/j.1750-3639.2001.tb00385.x

Micu, I., A. Ridsdale, L. Zhang, J. Woulfe, J. McClintock, C.A. Brantner, S.B. Andrews, and P.K. Stys. 2007. Real-time measurement of free Ca2+ changes in CNS myelin by two-photon microscopy. *Nat. Med.* 13:874–879. http://dx.doi.org/10.1038/nm1568

Mondino, A., and M.K. Jenkins. 1995. Accumulation of sequence-specific RNA-binding proteins in the cytosol of activated T cells undergoing RNA degradation and apoptosis. *J. Biol. Chem.* 270:26593–26601. http://dx.doi.org/10.1074/jbc.270.44.26593

Moujalled, D.M., W.D. Cook, T. Okamoto, J. Murphy, K.E. Lawlor, J.E. Vince, and D.L. Vaux. 2013. TNF can activate RIPK3 and cause programmed necrosis in the absence of RIPK1. *Cell Death Dis.* 4:e465. http://dx.doi.org/10.1038/cddis.2012.201

O'Meara, R.W., S.D. Ryan, H. Colognato, and R. Kothary. 2011. Derivation of enriched oligodendrocyte cultures and oligodendrocyte/neuron myelinating co-cultures from post-natal murine tissues. *J. Vis. Exp.* (54):3324.

Ofengeim, D., Y. Ito, A. Najafov, Y. Zhang, B. Shan, J.P. DeWitt, J. Ye, X. Zhang, A. Chang, H. Vakifahmetoglu-Norberg, et al. 2015. Activation of necroptosis in multiple sclerosis. *Cell Reports.* 10:1836–1849. http://dx.doi.org/10.1016/j.celrep.2015.02.051

Ousman, S.S., and S. David. 2000. Lysophosphatidylcholine induces rapid recruitment and activation of macrophages in the adult mouse spinal cord. *Glia.* 30:92–104. http://dx.doi.org/10.1002/(SICI)1098-1136(200003)30:1<92::AID-GLIA10>3.0.CO;2-W

Ousman, S.S., and S. David. 2001. MIP-1alpha, MCP-1, GM-CSF, and TNF-alpha control the immune cell response that mediates rapid phagocytosis of myelin from the adult mouse spinal cord. *J. Neurosci.* 21:4649–4656.

Padmanabhan, P.K., M. Samant, S. Cloutier, M.J. Simard, and B. Papadopoulou. 2012. Apoptosis-like programmed cell death induces antisense ribosomal RNA (rRNA) fragmentation and rRNA degradation in *Leishmania*. *Cell Death Differ.* 19:1972–1982. http://dx.doi.org/10.1038/cdd.2012.85

Plemel, J.R., M.B. Keough, G.J. Duncan, J.S. Sparling, V.W. Yong, P.K. Stys, and W. Tetzlaff. 2014. Remyelination after spinal cord injury: is it a target for repair? *Prog. Neurobiol.* 117:54–72. http://dx.doi.org/10.1016/j.pneurobio.2014.02.006

Richter-Landsberg, C., and U. Vollgraf. 1998. Mode of cell injury and death after hydrogen peroxide exposure in cultured oligodendroglia cells. *Exp. Cell Res.* 244:218–229. http://dx.doi.org/10.1006/excr.1998.4188

Schoenberg, D.R., and L.E. Maquat. 2012. Regulation of cytoplasmic mRNA decay. *Nat. Rev. Genet.* 13:246–259. http://dx.doi.org/10.1038/nrg3254

Scurlock, B., and G. Dawson. 1999. Differential responses of oligodendrocytes to tumor necrosis factor and other pro-apoptotic agents: Role of ceramide in apoptosis. *J. Neurosci. Res.* 55:514–522. http://dx.doi.org/10.1002/(SICI)1097-4547(19990215)55:4<514::AID-JNR11>3.0.CO;2-V

Seo, J., E.W. Lee, H. Sung, D. Seong, Y. Dondelinger, J. Shin, M. Jeong, H.K. Lee, J.H. Kim, S.Y. Han, et al. 2016. CHIP controls necroptosis through ubiquitylation- and lysosome-dependent degradation of RIPK3. *Nat. Cell Biol.* 18:291–302. http://dx.doi.org/10.1038/ncb3314

Sosna, J., S. Voigt, S. Mathieu, D. Kabelitz, A. Trad, O. Janssen, C. Meyer-Schwesinger, S. Schütze, and D. Adam. 2013. The proteases HtrA2/Omi and UCH-L1 regulate TNF-induced necroptosis. *Cell Commun. Signal.* 11:76. http://dx.doi.org/10.1186/1478-811X-11-76

Taatjes, D.J., B.E. Sobel, and R.C. Budd. 2008. Morphological and cytochemical determination of cell death by apoptosis. *Histochem. Cell Biol.* 129:33–43. http://dx.doi.org/10.1007/s00418-007-0356-9

Tomita, G. 1967. Fluorescence-excitation spectra of acridine orange-DNA and -RNA systems. *Biophysik.* 4:23–29. http://dx.doi.org/10.1007/BF01188503

Traganos, F., Z. Darzynkiewicz, T. Sharpless, and M.R. Melamed. 1977. Simultaneous staining of ribonucleic and deoxyribonucleic acids in unfixed cells using acridine orange in a flow cytofluorometric system. *J. Histochem. Cytochem.* 25:46–56. http://dx.doi.org/10.1177/25.1.64567

Vanden Berghe, T., S. Grootjans, V. Goossens, Y. Dondelinger, D.V. Krysko, N. Takahashi, and P. Vandenabeele. 2013. Determination of apoptotic and necrotic cell death in vitro and in vivo. *Methods.* 61:117–129. http://dx.doi.org/10.1016/j.ymeth.2013.02.011

Vercammen, D., R. Beyaert, G. Denecker, V. Goossens, G. Van Loo, W. Declercq, J. Grooten, W. Fiers, and P. Vandenabeele. 1998. Inhibition of caspases increases the sensitivity of L929 cells to necrosis mediated by tumor necrosis factor. *J. Exp. Med.* 187:1477–1485. http://dx.doi.org/10.1084/jem.187.9.1477

Wagner, A. 2005. Energy constraints on the evolution of gene expression. *Mol. Biol. Evol.* 22:1365–1374. http://dx.doi.org/10.1093/molbev/msi126

Wyllie, A.H., J.F. Kerr, and A.R. Currie. 1980. Cell death: The significance of apoptosis. *Int. Rev. Cytol.* 68:251–306. http://dx.doi.org/10.1016/S0074-7696(08)62312-8

Zhang, Y., K. Chen, S.A. Sloan, M.L. Bennett, A.R. Scholze, S. O'Keeffe, H.P. Phatnani, P. Guarnieri, C. Caneda, N. Ruderisch, et al. 2014. An RNA-sequencing transcriptome and splicing database of glia, neurons, and vascular cells of the cerebral cortex. *J. Neurosci.* 34:11929–11947. http://dx.doi.org/10.1523/JNEUROSCI.1860-14.2014